Science of Remote Sensing 10 (2024) 100165

Contents lists available at ScienceDirect

Science of Remote Sensing

journal homepage: www.sciencedirect.com/journal/science-of-remote-sensing

Enhancing burned area monitoring with VIIRS dataset: A case study in Sub-Saharan Africa

Boris Ouattara [a,b], Michael Thiel [c,*], Barbara Sponholz [a], Heiko Paeth [a], Marta Yebra [d,e], Florent Mouillot [f], Patrick Kacic [c], Kwame Hackman [g,h]

[a] Department of Physical Geography, Institute of Geography and Geology, University of Würzburg, 97074, Würzburg, Germany
[b] Institute of Climate-Smart Agriculture, Thuenen Institute, 38116, Brunswick, Germany
[c] University of Würzburg, Institute of Geography and Geology, Department of Remote Sensing, John Skilton Str. 4a, 97074, Würzburg, Germany
[d] Fenner School of Environment and Society, The Australian National University, Canberra, ACT 2601, Australia
[e] School of Engineering, College of Engineering and Computer Science, The Australian National University, Canberra, ACT, 2600, Australia
[f] UMR CEFE 5175, Centre National de la Recherche Scientifique, Université de Montpellier, Université Paul-Valéry Montpellier, Ecole Pratique des Hautes Etudes, Institut de Recherche pour le Développement, 1919 route de Mende, 34293, Montpellier, Cedex 5, France
[g] Data Management Department, WASCAL Competence Center, Ouagadougou, 06 BP 9507, Burkina Faso
[h] Department of Environmental Management, University of Energy and Natural Resources, Sunyani, BS-0061-2164, Ghana

A R T I C L E I N F O

Keywords:
Burned area mapping
VIIRS
Active fires
Google earth engine
Africa

A B S T R A C T

Since 2001, the Moderate Resolution Imaging Spectroradiometer (MODIS) sensor on board the Aqua and Terra platforms has made great strides in providing information on global burned areas (BA). However, the MODIS mission is nearing its end. The Visible Infrared Imaging Radiometer Suite (VIIRS) sensors, presented as the MODIS Aqua heritage, could be an excellent alternative to ensure the temporal continuity of this information at a moderate resolution. This paper describes and evaluates the effectiveness of our developed hybrid algorithm, which utilizes VIIRS reflectance and active fire products on the Google Earth Engine platform, in producing efficient information about BA. The study investigates the algorithm's performance in sub-Saharan Africa as the region of interest in 2019, using biweekly outputs and a spatial resolution of 250 m. The algorithm encompasses several steps, including pre-processing individual scenes, creating cloud-free composites, generating binary reference data for burned and non-burned areas, conducting a supervised classification using random forest, and performing region shaping. The VIIRS-BA final product, which includes three confidence levels (low, moderate, and high) known as the uncertainty layer, is compared to four other burned area products. The validation is conducted against 27 reference sampling units from the Sentinel-2 Burned Area Reference Database dataset, allowing for a comprehensive uncertainty assessment across five various biomes. The VIIRS-BA product identified 5.1 million km^2 of BA, which was significantly larger than other global coarse resolution BA products such as FireCCI51, FireCCIS310, and MCD64A1 and close to the fine resolution FireCCISFD20 with a difference of 7.3%. The differences were less significant in biomes such as “Tropical Savannas” and “Temperate Grasslands” which are characterized by persistent biomass burning. Based on a stratified random sampling, the validation results demonstrate varying levels of accuracy for the VIIRS-BA product across different confidence levels. The commission error (CE) ranges from 7.8% to 23.4%, while the omission error (OE) falls between 29.4% and 58.8%. Notably, there is a significant reduction in OE (ranging from 40.7% to 50.5%) compared to global BA products like FireCCI51, FireCCIS310, and MCD64A1. When compared to VIIRS-BA, the FireCCISFD20 regional product has a 37% better OE performance. While VIIRS-BA shows great potential in detecting fires that global products miss, the VIIRS-BA with low confidence level tends to overestimate BA in regions with high fire activity. To address this, future versions of the algorithm will integrate the updated VIIRS reflectance data alongside VIIRS active fire from the National Oceanic and Atmospheric Administration to reduce CE and improve understanding spatial patterns.

* Corresponding author.
E-mail address: michael.thiel@uni-wuerzburg.de (M. Thiel).

https://doi.org/10.1016/j.srs.2024.100165
Received 8 April 2024; Received in revised form 28 August 2024; Accepted 16 September 2024
Available online 21 September 2024

1. Introduction

Biomass combustion by wildfires is considered as a major component of the terrestrial carbon cycle and a substantial source of greenhouse gas emissions (Kumar et al., 2022; Vernooij et al., 2021). In addition, fires influence plant species functioning and dynamic (Pathak et al., 2017), land use (Frost et al., 2020; Van Wees et al., 2022), soil erosion, and hydrological cycles (Rostami et al., 2022) and other societal impacts as air pollution, human health and assets (Schneider et al., 2021; Xie et al., 2022), now increasingly assembled in fire risk assessment frameworks (Chuvieco et al., 2023).

Satellite-derived burned area (BA) and active fires data are used to analyse spatiotemporal patterns of fire activity, providing valuable insights into the drivers behind fire occurrence (Haas et al., 2022), its impacts (Ramo et al., 2021), and numerous diverse purposes (Chuvieco et al., 2019; Mouillot et al., 2014). A major field of research using global BA is climate modelling given fire disturbance defined as part of the Essential Climate Variables (GTOS, 2009; GCOS, 2016), and a keystone information vegetation model benchmarking (Hantson et al., 2016). More specifically, BA and active fires statistics are essential for atmospheric emission models and combustion characteristics (Kaiser et al., 2012; Van Der Werf et al., 2017). However, quick access to BA information at both local and global levels enabled the identification of other relevant users (Mouillot et al., 2014). Wildfire managers and related services use fire history to assess fire risk and apply risk reduction measures; insurance companies and health planners may benefit from modelled fire impacts on human health (Uda et al., 2019) and safety of properties (Bowman et al., 2017; Moritz et al., 2014), derived from BA data; policymakers can monitor progress in sustainable development goals (Honeck et al., 2018).

In the context of fire monitoring and management, several institutions and/or countries are contributing to the development of mapping-based resources for systematic assessment of BA. In the early 2000s, the Joint Research Centre of the European Union produced the first global BA product, called Global Burned Area (Tansey, 2004). Simultaneously, the European Space Agency (ESA) developed the GLOBSCAR BA product (Simon, 2004). They were both based on the SPOT Vegetation (VGT) sensor with 1 km^2 resolution. NASA has a long-standing history of global BA assessment using the Moderate Resolution Imaging Spectroradiometer (MODIS) sensor, with a latest collection of BA products (MCD64A1) at 500 m resolution (Giglio et al., 2018). According to Lizundia-Loiola et al. (2020) research, the FireCCI51 (based on MODIS data at 250 m), from the Fire_cci project part of ESA's Climate Change Initiative program, is currently the most accurate among existing global BA products at moderate spatial resolution.

In a step forward using new sensors, Lizundia-Loiola et al. (2022) used Copernicus Sentinel-3 Synergy data and demonstrated that, by incorporating various inputs including moderate spatial resolution as the primary input, they successfully identified more than 1 million km^2 of BA that remained undetected by FireCCI51. That study highlighted one of the major limitations of those precursor global BA products, specifically, that the base spatial resolution of these products was larger than the size of many fires, therefore omitted in the total BA. Randerson et al. (2012) used MCD64A1 product to find that approximately 25% of global BA are small fires that are not captured in the data. Similarly, other studies found that up to 55% of total BA are comprised of small fire patches that are completely absent from the data for Africa (Ramo et al., 2021; Roteta et al., 2019). Accuracy evaluations of these BA products showed that, on average, the omission rate was considerably higher than the commission rate, reaching up to 70% (Boschetti et al., 2019; Lizundia-Loiola et al., 2020). The use of higher spatial resolution data now available from the new generation of satellite sensors appears as an alternative to fill these gaps and should increase the detection threshold and include these small fires.

Various approaches have been experimented with the main goal to accurately delineate BA using medium spatial resolution (between 10 and 30 m) (Roteta et al., 2021a; Tanase et al., 2020), including integrating different sensors such as optical and radar (Belenguer-Plomer et al., 2021), and merging higher spatial resolution datasets such as Landsat and Sentinel-2 (S2) into a single algorithm (Abdikan et al., 2022; Ngadze et al., 2020; Roy et al., 2019). These efforts have yielded encouraging outcomes regarding their spatial precision. However, these previous studies creating BA products have mostly been limited to well-defined geographical contexts (Chuvieco et al., 2022; Pinto et al., 2021). The development of a BA product at global scale requires significant data storage and processing capabilities. Additionally, it is worth noting that even with improved spatial resolution, not all small fires can be detected. In addition, daily temporal coverage for accurate identification of the burning dates is a pre requisite for accurate biosphere/atmosphere interactions (Voulgarakis and Field, 2015), near real time delivery (Urbanski et al., 2018), daily fire-weather relationships (Potter and McEvoy, 2021), and accurate time-dependent pixel aggregation into fire patches (Moreno and Mouillot, 2021). This becomes even more crucial in tropical ecosystems where cloud cover is persistent and the post-fire signal is brief inducing delays in reflectance change detection (Lasko, 2019). An additional issue remains on agricultural burnings, often small in size and fast spreading, where high-resolution imagery should be available at least once a day (Hall et al., 2021). The huge processing effort and the limited temporal resolution of medium spatial resolution sensors (8 days if both Landsat-7 and 8 are used, and up to 3–5 days at best if we combine Sentinel-1 and S2) mean that global BA products still heavily rely on moderate spatial resolution sensors with 250–500 m pixel sizes and 1–2 days revisit time.

With the end of the MODIS lifetime, the scientific community is facing a challenging situation (Smith, 2022). The adaptation of MODIS-based algorithms and products to new satellites and sensors is necessary to ensure the provision and continuity of BA products in the future. One potential solution is the use of Visible Infrared Imaging Radiometer Suite (VIIRS) onboard the Suomi National Polar-orbiting Partnership and NOAA-20 satellites to replace the 1:30am/pm MODIS Aqua data stream. VIIRS has been developed based on the experience gained from previous sensors developments, particularly MODIS. It has a large image swath (~3040 km wide) and a relatively short revisit time, which ensures at least two observations a day in 22 spectral bands at 375 m and 750 m. Two active fires detection products are currently produced based on VIIRS data (Csiszar et al., 2014; Schroeder et al., 2014). Several studies have shown that VIIRS has the potential to replace MODIS as a viable alternative for global BA mapping (Fernández-Manso and Quintano, 2020; Li et al., 2020). To ensure the development of high-quality global BA products, further testing and validation of VIIRS data is needed.

This paper describes the development of a new global BA algorithm called VIIRS-BA, which solely relies on the VIIRS reflectance and active fires products and is run in Google Earth Engine (GEE) (Gorelick et al., 2017). While GEE has been used for over a decade (L. Wang et al., 2020), there has been limited research on global BA using this tool (Daldegan et al., 2019; Roteta et al., 2021a; Seydi et al., 2021). Given the rich satellite databases and the ability to process large-scale information available in GEE, it represents an effective choice for our methodology. We used the random forest (RF) algorithm (Breiman, 2001) as a machine learning approach in GEE to develop our hybrid algorithm for detecting BA at 250 m resolution every 15 days. RF offers advantages over other machine learning algorithms such as artificial neural networks, support vector machines, and recurrent neural networks in BA detection, thanks to its ability to manage high-dimensional and noisy datasets, and provide feature importance rankings (Mashhadi and Alganci, 2021). Moreover, RF has demonstrated promising results by effectively handling the spectral response complexities of burned areas (Roteta and Oliva, 2020).

In the following sections, we provide a detailed explanation of the algorithm, its implementation, and the choice of the final spatial resolution of the VIIRS-BA product. (section 2.3), along with its accuracy to map BA in that region (section 2.4). We provide an overview of our BA products at different confidence levels (section 3.1). We also compared the distribution of the BA generated by VIIRS-BA with other contemporary products such as FireCCI51, FireCCIS310, FireCCISFD20 and MCD64A1 products (section 3.2). The reasons for selecting these datasets are based on their ability to meet at least two of the following three criteria for end-user products.

(1) spatial resolution: these datasets offer spatial resolutions similar to the intended new BA products;
(2) temporal resolution: they provide consistent time series data, with at least monthly updates, which is essential for temporal comparisons on a monthly basis;
(3) area coverage: these datasets cover the selected study area used to evaluate the VIIRS-BA product, which is Sub-Saharan Africa (SSA), ensuring comprehensive spatial analysis.

Additionally, we performed validation using a robust reference dataset from the Burned Area Reference Database (BARD) in different biomes, produced specifically for SSA (Stroppiana et al., 2022) (section 3.3). Our study focused on the year 2019 because, at the time of writing this manuscript, the other BA products required for comparison were primarily available only/up to that year.

2. Study area and data

2.1. Study area

The VIIRS-BA Algorithm has been tested in SSA, excluding Madagascar, which is depicted in Fig. 1. Fire patterns in Africa vary across different regions and are influenced by a combination of climatic, ecological, and anthropogenic factors (Haliuc et al., 2023). Human activities, such as crop management, grazing, and hunting, are the primary causes of fires in this region (Grégoire et al., 2013; Lewis et al., 2015). Africa has the highest BA compared to any other region in the world (up to 70%) (Giglio et al., 2013; Chuvieco et al., 2018). According to Ramo et al. (2021), the area burned by fires in Africa each year is comparable to the size of Europe. Africa is crucial in global carbon emissions, contributing nearly half of all carbon released by landscape fires annually (Van Der Werf et al., 2010), estimated at approximately 1.0 (±0.22) petagrams of carbon per year (Valentini et al., 2014). African fires account for about 30%–50% of the total biomass burned worldwide each year. However, the conversion of natural vegetation to croplands due to land cover changes has led to a decrease in the total BA (Grégoire et al., 2013; Andela et al., 2017).

Section 2.2 further elaborates on the major classification of biomes in this area. Fires predominantly occur during the dry season in both the Northern and Southern African hemisphere (NHAF, SHAF), ranging from October to March north of the Equator and from May to October in the south (Chuvieco et al., 2022).

2.2. Satellite datasets

An overview of the satellite datasets used in this study, including surface reflectance data, active fires data, and land use/land cover (LULC) data, are presented in Table 1.

2.2.1. VIIRS surface reflectance and active fires/hotspots data

The Visible Infrared Imaging Radiometer Suite (VIIRS) instruments are aboard the Suomi National Polar-orbiting Partnership (Suomi NPP) and National Oceanic and Atmospheric Administration (NOAA-20) satellites. For the present study, only VIIRS data from Suomi NPP were used as it provides a daily time series beginning in January 2012, while the NOAA-20 data only became available from January 2020. VIIRS collects visible and infrared imagery and global observations of land, atmosphere, cryosphere, and oceans.

The surface reflectance (VIIRS-SR) dataset used in this study is the VNP09A1 collection 1 product (Vermote et al., 2014). It has five resolution imagery channels (bands I1 to I5) with 32 detectors each, 16 moderate resolution channels (bands M1 to M16), and a panchromatic day–night band (DNB) with 16 detectors each. The nominal spatial resolution is 375 m for the I bands and 750 m for the M bands and the DNB. It is directly available in the GEE environment were the I bands are resampled to 500 m and M bands to 1 km. These bands were used to

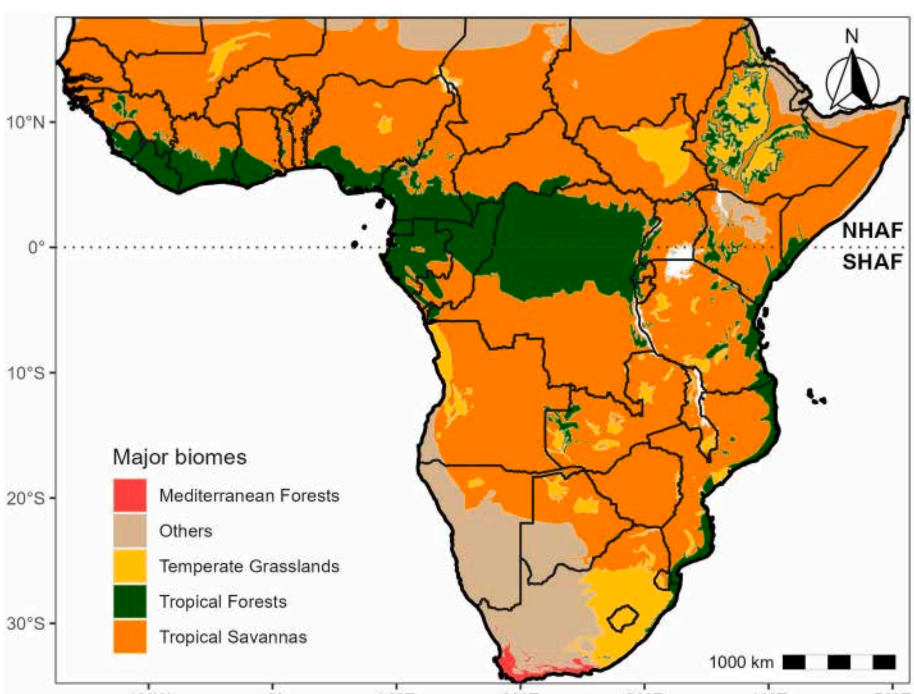

Fig. 1. Study area with the subdivision of the Northern and Southern African hemisphere (NHAF, SHAF) according to the GFED regionalization (Van Der Werf et al., 2017) and the reclassified (Olson et al., 2001) major biomes.

Table 1
List of satellites dataset used in this study. MCD64A1, FireCCI51 and FireCCIS310 and FireCCISFD20 were used for comparison.

Satellite/Product	Sensor	Description	Product Code (collection/version)	Resolution		Availability
				Spatial	Temporal	
Suomi NPP	VIIRS	Surface Reflectance	VNP09GA (collection 1)	375 m	daily	from 2012
Suomi NPP	VIIRS	Active Fire	VNP14IMGML (collection 1)	375 m	daily	from 2012
Terra/Aqua	MODIS	Land Cover	MCD12Q1 (version 6.1)	500 m	annual	from 2000
Terra/Aqua	MODIS	Burned Area	MCD64A1 (collection 6)	500 m	daily	from 2000
Terra/Aqua	MODIS	Burned Area	FireCCI51 (version 5.1)	250 m	daily	from 2001
Sentinel-3 Synergy	Sentinel-3 OLCI and SLSTR	Burned Area	FireCCIS310 (version 1.0)	300 m	daily	2019
Sentinel-2	Sentinel-2 MSI	Burned Area	FireCCISFD20 (version 2.0)	20 m	daily	2019

derive vegetation indices and the tasselled cap transformation (section 2.3.2).

VIIRS 375 m active fires product VNP14IMGML (Schroeder et al., 2014) is also used. This product was designed using VIIRS 375 m (I bands) channels and can be downloaded from the Fire Information for Resource Management System (FIRMS) website since it is not yet available in GEE (FIRMS, last accessed March 2023). The VIIRS data complement the MODIS fire detections but have improved spatial resolution and night-time performance (Justice et al., 2013). It represents the center of a 375 m pixel and provides a more sensitive response to fires on relatively small areas, as well as improved mapping of large fire perimeters, making it well-suited for use in support of fire management and other scientific applications requiring improved fire mapping fidelity (Li et al., 2018).

For this study, available daily VIIRS-SR and VIIRS active fires (VIIRS-AF) data for the year 2019 in sub-Saharan Africa were used.

2.2.2. Land cover and biome data

Global land cover classification datasets derived from remote sensing technology are continuously being developed, providing valuable information at regional and global scales. For our BA algorithm, we utilized the MODIS Land Cover Type MCD12Q1 version 6.1, which characterizes five global land cover classification systems (Hansen et al., 2000). These systems describe land cover properties derived from observations spanning a year's input of observation data from the Terra and Aqua satellites. The MODIS LULC map was chosen over other LULC data available on GEE, which had a higher spatial resolution, because of its longer coverage period (from 2001 to 2021) and consistent annual update. For consistency in future assessments of fire emissions using the derived BA product, we made a deliberate choice to opt for the University of Maryland's level 3 product (Friedl and Sulla-Menashe, 2022), which comprises 15 distinct LULC classes. The reason behind selecting this LULC data was that it closely aligns with the fire type classes identified by Akagi et al. (2011).

The Olson's Biomes dataset originally contained 16 different biomes, which were later reclassified into 7 major biomes to simplify the assessment of BA across different regions. As a result of this reclassification, five major biomes were identified for the SSA region (Fig. 1). The original and final biome names are provided in Table 2.

Table 2
Reclassification of the eight original categories from Olson et al. (2001)'s biomes classification in the study area.

New categories	Original biome categories
Mediterranean Forests	Mediterranean forests woodlands and scrub
Others	Deserts and xeric shrublands Mangroves
Temperate Grasslands	Flooded grasslands and shrublands Montane grasslands and savannas
Tropical Forests	Tropical as subtropical moist broadleaf forests Tropical as subtropical dry broadleaf forests
Tropical Savannas	Tropical and subtropical grasslands savannas and shrublands

2.2.3. Global/regional burned area products

The product derived from this research (VIIRS-BA) was compared to four current state-of-the-art BA products. These included three global BA products: MCD64A1 (Giglio et al., 2018), FireCCI51 (Chuvieco et al., 2018), and FireCCIS310 (Lizundia-Loiola et al., 2022), as well as a regional BA product at fine resolution, FireCCISFD20 (Chuvieco et al., 2022).

MCD64A1 and FireCCI51 are both based on surface reflectance measurements and standard products generated by the MODIS sensors onboard the Terra and Aqua satellite platforms, covering a common period from 2001 to 2019. MCD64A1 detects and maps daily fires at 500 m by combining MODIS Terra and Aqua daily surface reflectance products with MODIS active fires data. FireCCI51 provides higher spatial resolution at 250 m and was developed to complement existing BA products. It identifies and maps BA by integrating daily Terra MODIS red and near-infrared reflectance measurements and MODIS monthly active fires data. FireCCIS310 is a new product that uses a hybrid algorithm based on Copernicus Sentinel-3 Synergy (SYN) data and VIIRS-AF for global detection of BA. It relies on SYN shortwave infrared bands to compute a multi-temporal separability index and active fires from the VIIRS sensor to generate spatio-temporal clusters for determining local detection thresholds. FireCCIS310 overcomes some limitations of the precursor FireCCI51 product, particularly the low temporal reporting accuracy and border effects between tiles. The FireCCISFD20 algorithm utilizes S2 MSI and VIIRS-AF to produce a 20 m BA output. The algorithm compares S2 tiles using six variables and two spectral indices, generating two independent products that are merged to obtain the final output. Each scene is compared to the previous four scenes to complete areas masked as not burnable.

3. Methods

3.1. Burned area framework

The algorithm developed in this study relies on VIIRS-SR and VIIRS-AF to generate biweekly BA at 250 m resolution from 2012 onwards. Our study was restricted to the year 2019, as the others BA products required for comparison are predominantly accessible up to/only to that year. Furthermore, analysing results conducted with these products in the same year would be more convenient.

GEE easily handles the combination of bands with different spatial resolutions by automatically adjusting for resolution differences during processing (Google Developers, last accessed March 2024). This built-in feature streamlines data processing and ensures user-friendly operations. GEE performed all preprocessing and calculations to derive the VIIRS-BA product, while R software generated the analysis, graphs, and maps.

During the export stage, users can customise the output spatial resolution to meet their specific needs. However, two challenges arise when deciding on our final product's spatial resolution. The final choice is not arbitrary. Choosing a spatial resolution lower than 250 m exceeds the memory limit of GEE. Therefore, the dilemma lies in selecting the original or resampled spatial resolution within GEE for the inputs. This decision involves considering the inherent resolutions of the Suomi NPP sensor (375 m, 500 m, 750 m, or 1 km) based on the following information.

- VIIRS-AF: 375 m
- original VIIRS-SR: I bands 375 m or M bands 750 m
- resampled VIIRS-SR in GEE: I bands 500 m or M bands 1 km.

Options involving spatial resolutions greater than 500 m (750 m, 1 km) were rejected. For comparison purposes, the goal is to have at least one spatial resolution similar to that of the currently available BA products.

We then conducted prior tests to evaluate how the final VIIRS-BA spatial resolution affects accuracy and BA detection capability. Appendix A1 provides the methodology and results of these tests. We compared VIIRS-BA images at three different spatial resolutions: 250 m, 375 m, and 500 m. The 250 m spatial resolution did better in these preselection tests than the 375 m and 500 m. This supports what Boschetti et al. (2004) found about how low spatial resolution affects the accuracy of the BA product and the idea of "low-resolution bias".

The workflow of the BA algorithm can be summarized as follows: (1) pre-processing of individual scenes, (2) creating cloud-free composites of pre-fire and post-fire images, (3) generating a binary classification of fire and no-fire pixels and creating a training dataset, (4) applying a supervised classification using RF with burned/unburned core data as response and spectral indices as predictors, and (5) applying post-processing steps to filter small isolated BA and fill gaps in larger BA (Fig. 2). The final VIIRS-BA product is compared to some global BA products and validated against BARD reference dataset.

3.1.1. *Pre-processing*

The main input underwent several processing steps, including cloud masking, filtering, and reclassification.

The GEE platform provides a surface reflectance quality flag band called QF1 for VIIRS-SR, which contains cloud mask information. To ensure the quality of the cloud mask, cloud detection and confidence levels were evaluated. Only the clear-sky pixels labelled as "Confident clear" in cloud detection and confidence and "High" in cloud mask quality were selected, based on the QF1 parameter.

The VIIRS-AF data was filtered based on specific conditions related to hotspot detection (Schroeder and Giglio, 2018). Non-fire related hotspots, such as those from active volcanoes, gas flares, and industrial burning, were removed using type-0 detections, which are presumed to be vegetation fires. Only high-confidence detections, representing pixels free of sun glint contamination, were included. The last condition required the fire radiative power to be greater than 0.

To improve the land filtering process in our algorithm, the MCD12Q1 LULC data was reclassified to obtain a binary image that represents vegetation and non-vegetation classes. The non-vegetation class includes areas classified as "urban" and "water".

3.1.2. *Image composite*

In the initial stage, a processing interval period is defined, consisting of a water mask period, pre-fire and post-fire periods, and a target period (Fig. 3).

The aim is to detect burn scars that occurred within a biweekly interval called the target period. It is important to note that in our study, a month can only have two target periods, and the first target period starts from the first day of the month and ends on the 15th day of the month. The second target period starts from the 16th day of the month and ends on the last day of the month, but it may not necessarily be 15 days. This paper uses this specific time interval for comparison with other products, but the algorithm can be applied to any biweekly interval. The pre and post-fire periods were based on the approach used by Liu et al. (2019), with the pre-fire period starting one month before and ending one month after the first day of the target period, and the post-fire period starting on the first day of the target period and ending one month after the first day of the target period.

To improve the accuracy of the results and remove noise, a composite image is created by combining the best features of each individual image. A per-pixel composite is performed on the cloud-masked VIIRS-SR to obtain a new set of VIIRS-SR that represents the best possible observation for each pixel during the number of days of that period. The pre-fire image collection is generated by compositing the maximum surface reflectance per pixel over the pre-fire period and the minimum surface reflectance per pixel for the post-fire period. This is based on the

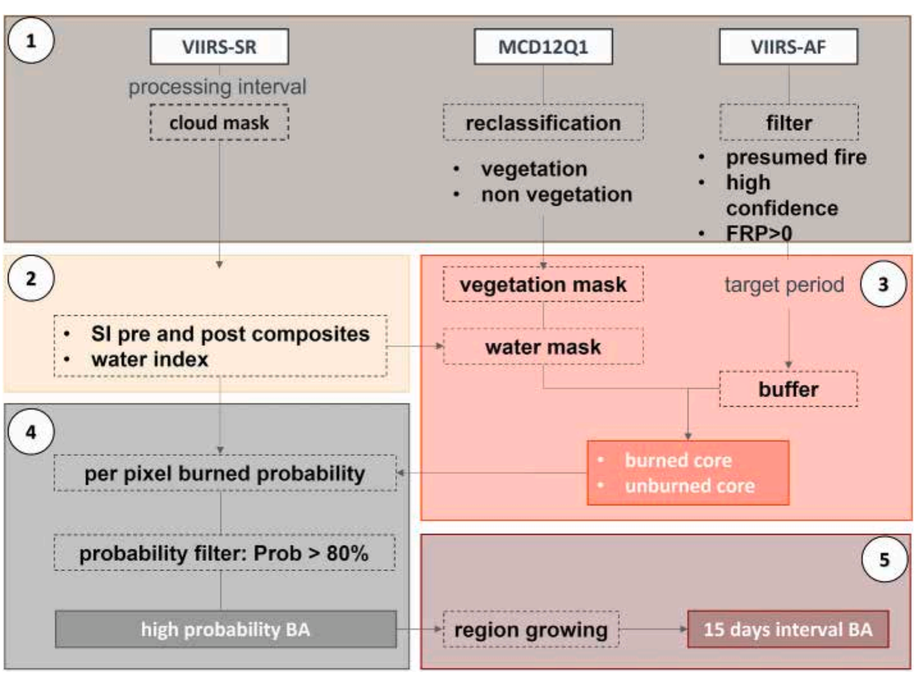

Fig. 2. Workflow of VIIRS-BA illustrating the process of mapping burned area using Google Earth Engine over a two-week interval. VIIRS-SR: VIIRS surface reflectance; VIIRS-AF: VIIIRS active fire; SI: spectral indices; FRP: fire radiative power.

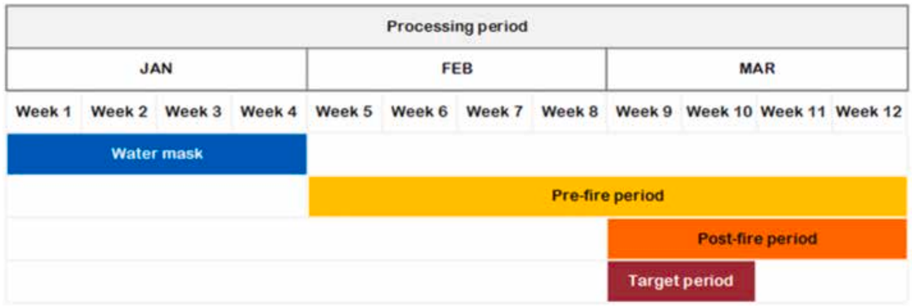

Fig. 3. The temporal location of different periods, in relation to the sample processing for the first 15 days of March.

assumption that BA generally have a high value for pre-fire and a low value for post-fire (Liu et al., 2019).

The water mask period corresponds to one month before the pre-fire period. A water mask is commonly used in biomass burning studies to eliminate the influence of water bodies and reduce false alarms in BA detection (Long et al., 2019). We utilize the Modified Normalized Difference Water Index (MNDWI; Xu, 2006) to generate the water mask. Numerous studies have shown the superior effectiveness of MNDWI in accurately extracting water surfaces compared to other indices like the Normalized Difference Water Index (NDWI) (Ali et al., 2019; Fattore et al., 2021).

Spectral indices (SI) play a crucial role in the detection of BA as they can capture specific spectral changes associated with fire and distinguish BA from unburned ones (Seydi et al., 2021; Szpakowski and Jensen, 2019). These indices exploit distinctive spectral signatures exhibited by BA, such as increased reflectance in the short-wave infrared (SWIR) and decreased reflectance in the visible and near-infrared (NIR) bands (Hu et al., 2021). The Tasselled Cap Transformation (TCT) is another valuable tool used in BA detection due to its ability to capture and differentiate changes in brightness, greenness, and wetness, which provide insights into different land covers and vegetation conditions, including BA (Filipponi, 2019; Simpson et al., 2016). In this study, various spectral indices were calculated for BA mapping, as presented in Table 3. A total of seven vegetation indices and three TCTs were utilized, covering most of the relevant spectrum for identifying burn scars using SWIR and/or NIR bands. These bands are known for their sensitivity to moisture content, enabling effective discrimination of BA (Al-Maliki et al., 2022; Frappart et al., 2018).

For each of the indices, we use the notation SI_{pre} and SI_{post} to describe any SI calculated from the pre-fire or the post-fire period, respectively (e.g., $NDVI_{pre}$), in the classification step.

They are computed as following.

(1) differenced normalized index (dSI)

$$dSI = SI_{pre} - SI_{post}$$

(2) ratio normalized index (rSI)

$$rSI = \frac{SI_{pre}}{SI_{post}} - 1$$

(3) relativised index (RSI)

$$RSI = \frac{dSI}{SI_{pre} + 1.001}$$

3.1.3. *Burned and unburned core*

Our algorithm uses the filtered VIIRS-AF dataset to select training pixels that are either burned or unburned, referred to as the burned and unburned core, respectively. Burned core pixels were originally identified as the center of the 375 m VIIRS-AF pixel. A 375 m buffer area around each point, representing the BA perimeter, is defined. This buffer distance may vary since technically, each active fire pixel would have a variable buffer based on its location in the swath layer. Indeed, the pixels at the edges of each swath may have a slightly different spatial resolution than those in the centre (Schroeder et al., 2014). However, this variation in spatial resolution is typically small enough that it does not significantly affect the delineation of the burned core surface. The vegetation and water masks from steps 1 and 2, respectively, were used as additional masks for the burned core to ensure that the burned core is located in the burnable LULC category.

Table 3
Spectral indices with formula used for the burned area mapping. At the bottom are the names of the spectral regions (in italics), the corresponding band names, and the centered wavelength in micrometers (in brackets).

Spectral indices/tasselled cap		Equation	Reference
Acronym	Full name		
NDVI	Normalized Difference Vegetation Index	$NDVI = \frac{NIR - Red}{NIR + Red}$	Rouse et al. (1973)
NDWI	Normalized Difference Water Index	$NDWI = \frac{Green - NIR}{Green + NIR}$	McFeeters (1996)
MNDWI	Modified Normalized Difference Water Index	$MNDWI = \frac{Green - SWIR2}{Green + SWIR2}$	Xu (2006)
NDMI	Normalized Difference Moisture Index	$NDMI = \frac{NIR - SWIR1}{NIR + SWIR1}$	Gao (1996)
NBR	Normalized Burn Ratio	$NBR = \frac{NIR - SWIR2}{NIR + SWIR2}$	Key and Benson (1999)
NBR2	Normalized Burn Ratio 2	$NBR2 = \frac{SWIR1 - SWIR2}{SWIR1 + SWIR2}$	Key and Benson (2006)
MIRBI	Mid-Infrared Burn Index	$MIRBI = 10 \times SWIR2 - 9.8 \times SWIR1 + 2$	Trigg and Flasse (2001)
BRI	Brightness	$BRI = (Blue \times 0.3037) + (Green \times 0.2793) + (Red \times 0.4743) + (NIR \times 0.5585) + (SWIR1 \times 0.5082) + (SWIR2 \times 0.1863)$	Kauth and Thomas (1976)
GRE	Greenness	$GRE = -(0.2848 \times Blue) - (0.243 \times Green) - (0.5436 \times Red) - (0.7243 \times NIR) - (0.0840 \times SWIR1) - (0.1800 \times SWIR2)$	Kauth and Thomas (1976)
WET	Wetness	$WET = (Blue \times 0.1509) + (Green \times 0.1973) + (Red \times 0.3279) + (NIR \times 0.3406) - (SWIR1 \times 0.7112) - (SWIR2 \times 0.4572)$	Kauth and Thomas (1976)

Blue: M3 (0.490 μm), *Green*: M4 (0.555 μm), *Red*: I1 (0.640 μm), *NIR*: I2 (0.865 μm), *SWIR1*: I3 (1.610 μm), *SWIR2*: M11 (2.25 μm).

To ensure that we only include potential burned pixels in burned core features, we apply a 10 km buffer around each fire hotspot. The pixels that fall within this buffer are excluded, while the ones outside of it are considered to be part of the unburned core.

Using a stratified random sampling strategy, we randomly select 20% of the burned core pixels and an equal number of unburned core pixels. The final burned and unburned samples are merged and divided into training (70%) and test (30%) sets for the RF model.

The major steps of the BA delineation are shown in Fig. 4.

3.1.4. Random forest model

The RF algorithm has gained popularity in remote sensing for the classification of BA due to its high accuracy and effectiveness in analyzing complex datasets with a large number of variables (Mashhadi and Alganci, 2021; Pacheco et al., 2021). Breiman (2001) proposed the RF technique, which is an ensemble classifier based on multiple decision trees for training and prediction. Each decision tree in the RF classifier acts as an independent base learner voting for sample predictions, allowing for better generalisation and more trustworthy classification results.

That algorithm is well-integrated into the GEE platform with the classification library of “ee.Classifier.smileRandomForest”. To perform the supervised image classification using RF, we utilized ten SI computed from the image composite. These included the differenced SI, ratio normalized SI, relativised SI, and post-fire SI, resulting in a total of 40 predictors used in the model. Previous studies have shown that various parameterization schemes of the RF model minimally affect the classification accuracy (Pelletier et al., 2016). To minimize computational load and achieve a relatively improved classification accuracy (Chen et al., 2021), the number of decision trees was set to 100, with the other parameters were set to default values. We configured the RF algorithm in “probability” mode for the classifier, which provided the probability (P) that a pixel was classified as “’burned”, allowing us to assess the confidence level of the classification. We trained the classifier using the burned and unburned core on the sampled predictors.

To define the confidence levels, we established three thresholds: low ($85\% > P \geq 80\%$), moderate ($90\% > P \geq 85\%$), and high ($P \geq 90\%$). The VIIRS-BA products in this study can be classified into three distinct categories based on their confidence levels. The naming conventions used for these confidence levels as standalone BA products are as follows.

(1) VIIRS-BA L, representing low confidence, includes pixels with low, moderate, and high probabilities of being burned ($85\% > P \geq 80\%$).
(2) VIIRS-BA M, indicating moderate confidence, consists of pixels with moderate and high probabilities of being burned ($90\% > P \geq 85\%$).
(3) VIIRS-BA H, denoting high confidence, exclusively contains pixels with high probabilities of being burned ($P \geq 90\%$).

3.1.5. Region growing

Once the confidence level is defined, we use growing region to balance commission and omission errors (Hardtke et al., 2015). It also helps to smooth and reduce the impact of small-scale noise and artifacts. This involves using a kernel filter to identify contiguous regions that have a high probability of being burned. Then, using a neighbourhood operation, we calculate the mode of the filtered probability within each connected region. This step allows us to assign a binary label of “burned” or “unburned” to each connected region based on a threshold value of the mode. Regions with a mode value above the threshold are classified as “burned”, while those with a mode value below the threshold are classified as “unburned”. A last label of “unobserved” is used for non-burnable areas such as water bodies and urban areas, which are identified using the MCD12Q1 LULC data and clouds mask within the target period.

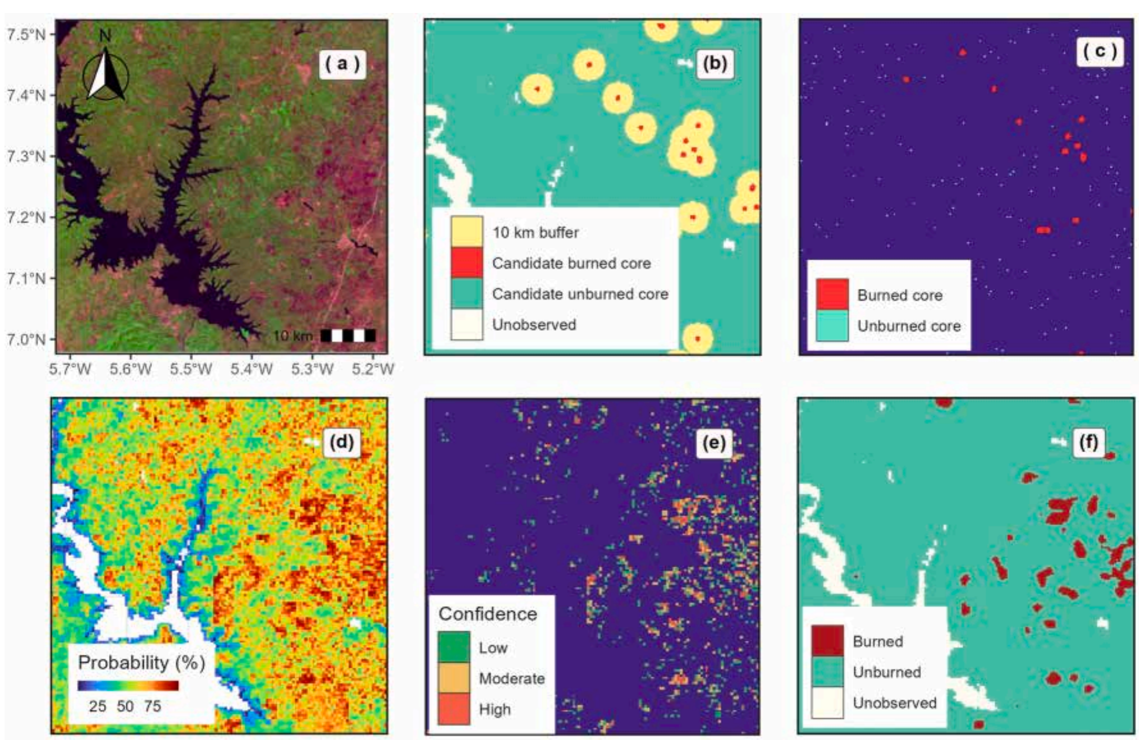

Fig. 4. Major steps associated with our burned area classification near Lake Kossou in central Cote d’Ivoire (West Africa). (a) Sentinel-2 image displayed in false colour composition (SWIR2, NIR, RED); (b) burned and unburned candidates; (c) burned and unburned cores; (d) burned probability; (e) burned area based on confidence level; (e) burned area map after region growing. (For interpretation of the references to colour in this figure legend, the reader is referred to the Web version of this article.)

3.2. Products performance

3.2.1. Burned area products intercomparison

After completing the annual analysis of VIIRS-BA, we further examined the VIIRS-BA based on the confidence level. Subsequently, a comparison was conducted between VIIRS-BA and other BA products, considering the BA fraction at a 0.25° grid resolution. The BA fraction represents the proportion of the land cover area within a grid that could potentially be affected by fire. We assessed spatial agreements and disparities between the products and performed a monthly distribution analysis to evaluate the comparison. Additionally, a detailed comparison at subset sites was conducted to highlight any potential local issues or differences.

3.2.2. Reference data

In any accuracy assessment of BA products, having representative and independent reference data is crucial. Such data should accurately represent the spatial and temporal distribution of surfaces affected by fire. The BARD is a significant advance in assessing the accuracy of BA products, as it provides a vetted set of reference sample sites (Franquesa et al., 2020). BARD compiles multitemporal global and regional burned area reference datasets for earth observation BA products validation.

To create a BARD for Sub-Saharan Africa, Stroppiana et al. (2022) used S2 time series images over 50 sampling units. The sampling units were designed to represent major fire regimes of the African continent in different ecoregions. A set of conditions was used to minimize cloud cover and to guarantee a minimum time lag between image pairs (Padilla et al., 2017). S2 image pairs were classified with a RF algorithm to provide burned perimeters, which were then combined to create a BA reference dataset. The dataset includes burned and unburned polygons as well as masked areas and is available online (BARD, last accessed March 2023).

The ecoregions were grouped in major biomes based on Olson et al. (2001). Stratified random sampling developed by Roteta et al. (2021b) was used to select 27 reference sampling units that represent all major biomes in SSA. The spatial distribution of these units is shown in Fig. 5. These reference sampling units provide accurate and representative data for assessing the accuracy of BA products in SSA. For the forthcoming section the sampling units will refer to validation areas (VA).

3.2.3. Accuracy assessment

Accuracy was assessed using the error matrix methodology described by Congalton (2001), and the following accuracy metrics were calculated: omission and commission error (OE, CE), Dice coefficient (DC), Jaccard Index (JI), Relative Bias (RelB), F-score (F1) and the Cohen's Kappa (Kappa). The accuracy measures were also analysed by main biome categories.

4. Results

4.1. VIIRS-BA product overview

An overview of the VIIRS-BA product for the year 2019 is presented in Fig. 6. Considering the lowest confidence level as the total BA detected by VIIRS-BA, the estimated BA amounts to 5.1 million km^2. When analysing the breakdown by confidence level solely, the respective BA detected for low, moderate, and high confidence levels are approximately 1.6 million km^2 (32%), 1.3 million km^2 (26%), and 2.1 million km^2 (42%) (Fig. 6a). Using the VIIRS-BA L product (low confidence level), the countries with the highest BA in NHAF are South Sudan, Central African Republic, Nigeria, and Chad, while in SHAF, they are Angola, the Democratic Republic of the Congo, Mozambique, and Zambia (Fig. 6b).

It is widely known that fires predominantly occur during the dry season in SSA. The period from November to February exhibits the highest fire activity in NHAF with a peak month in January, while fire activity in SHAF is observed from June to September with a peak in August, as indicated by the VIIRS-BA confidence products (Fig. 6c). When considering the confidence levels as individual BA products, the burned surface area decreases from low to high confidence levels for

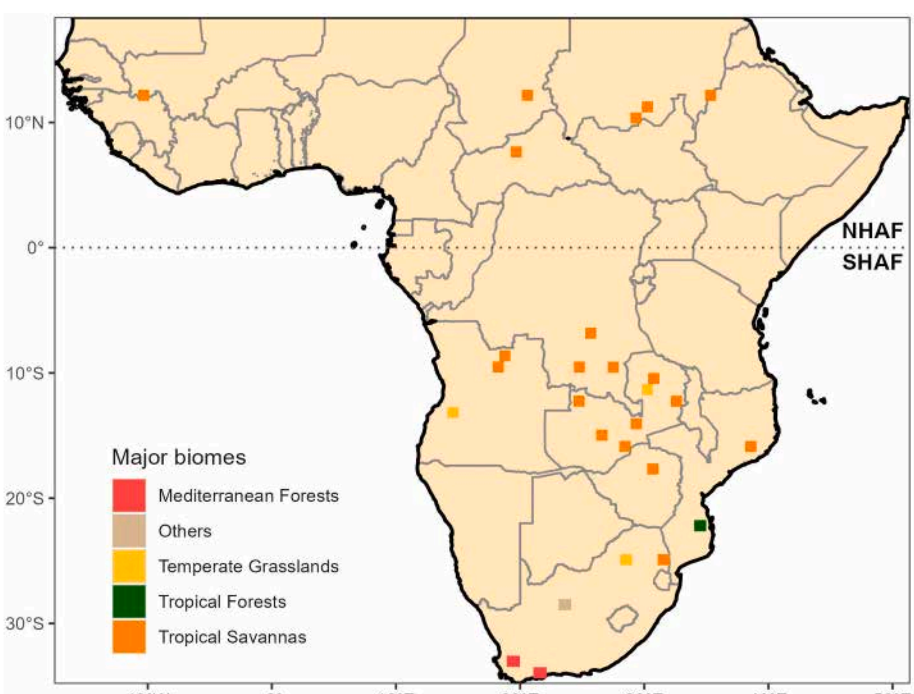

Fig. 5. Validation areas selected using a stratified random sampling methodology. These areas were based on a window size of 100 × 100 km, located at the center of the Sentinel-2 tile. The selection of the validation areas considered the major biomes present in each area. Mediterranean Forests: 34HCJ; 34HEH; Others: 34JGP; Temperate Grasslands: 33LVF; 35JPN; 35LRH; Tropical Forests: 36KXA; Tropical Savannas: 29PLP; 33LZK; 34LBR, 34NCP; 35LKG; 35LKK; 35LMD; 35LNK; 35LPC; 35LQE; 35MLN; 35PQM, 35PRN; 36JUT; 36KTF; 36LTP; 36LVM; 36PYU; 37LDC.

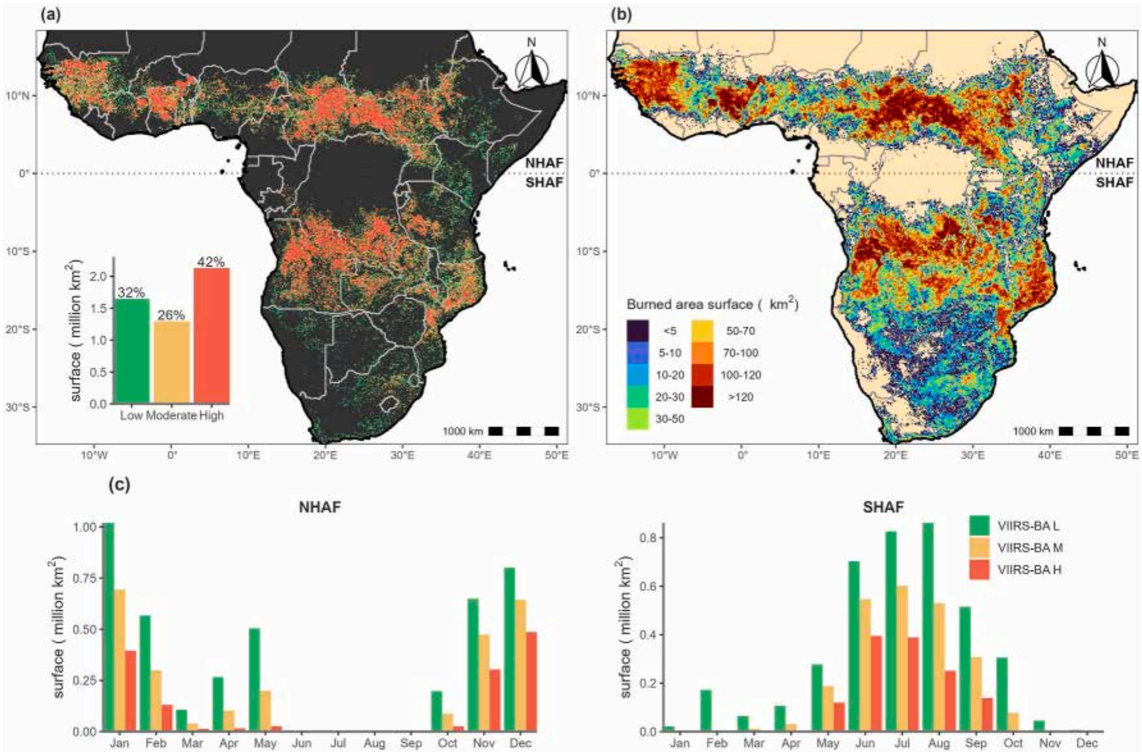

Fig. 6. Overview of the annual VIIRS-BA product for 2019. a) spatial distribution of VIIRS-BA L and its corresponding probability surface proportions; b) total burned area surface using VIIRS-BA L; c) monthly distribution of burned area in the Northern and Southern African hemispheres (NHAF, SHAF, respectively). VIIRS-BA L, VIIRS-BA M, VIIRS-BA H correspond respectively to VIIRS-BA product with low, moderate, and high confidence levels.

each month. A notable increase in BA is observed in April and May for NHAF and in February for SHAF when using the VIIRS-BA L product.

Among the top ten variables with the greatest importance in both regions (NHAF and SHAF), NDVI pre-fire and MNDWI post-fire stand out as having the highest values (Appendix A1). The indices NDMI, MIRBI, and MNDWI are the most frequently appearing in the top ten indices. As for index derivatives, it appears that none have significantly greater importance than the others; their contributions in the top 10 are quite similar. However, derivatives with the post-fire index appear one more time than both the pre-fire index and the differenced normalized index.

More than 80% of fires in SSA occur in “Tropical Savannas”, with less than 10% occurring in “Temperate Grasslands” (Table 4). Our analysis using the high-confidence product (VIIRS-BA H) reveals that over 2 million km^2 (93%) of the burned surface in SSA corresponds to “Tropical Savannas”. However, this accounts for less than 10% of the total surface area of that biome.

4.2. Comparison with existing burned area products

4.2.1. Spatial pattern

In 2019, the VIIRS-BA product (with lowest confidence level) detected a total BA of 5.1 million km^2, which was significantly larger than most of the BA estimated by other products in SSA. Specifically, it was 97.6% larger than the FireCCI51 product (2.6 million km^2), 73.5% larger than the FireCCIS310 product (2.9 million km^2), and 138.7% larger than the MCD64A1 product (2.1 million km^2). However, the difference between the VIIRS-BA product and the FireCCISFD20 product (4.7 million km^2) was relatively small, with a difference of 7.3%.

Table 4
Burned area (10^3 km^2) and the percentage contribution of each biome to the total burned area (in bold) for each confidence level (L: Low, M: Medium, H: High) in VIIRS-BA product.

	VIIRS-BA L		VIIRS-BA M		VIIRS-BA H	
Mediterranean forests	17.5	**1.1**	1.5	**0.1**	0.2	**<1**
Others	64.3	**3.9**	6.6	**0.5**	1.7	**0.1**
Temperate grasslands	135.3	**8.2**	83.6	**6.5**	87.9	**4.1**
Tropical savannas	1318.9	**80.1**	1130.0	**87.3**	1986.2	**93.2**
Tropical forests	111.3	**6.8**	72.2	**5.6**	54.0	**2.5**
Total	1647.3		1293.9		2130.0	

When comparing fire activity at a 0.25° grid resolution, all five products exhibited similar spatial patterns for both high and low fraction values, as shown in Fig. 6. However, the VIIRS-BA product consistently showed a significantly higher BA fraction in many regions compared to the other products (Fig. 7a–e), particularly in areas with persistent biomass burning like “Tropical Savannas” and “Temperate Grasslands”. The difference in observed BA fraction highlights a significant underestimation in the other inventories when using these satellite products. This underestimation is particularly striking, with a discrepancy of over 80% in areas with high fire activity, especially in NHAF regions such as Guinea, the Central African Republic, and South Sudan. A similar trend can be observed in SHAF regions, specifically near Mozambique. Nevertheless, in specific biome like the “Tropical Forest” in West and Central Africa, FireCCIS310 and FireCCISFD20 detected noticeably more BA compared to the other products.

Regardless of the BA fraction values, the spatial agreement among the different BA products was found to be moderate at 51% (Fig. 7f). This indicates that there is a considerable degree of variation and inconsistency among the products in delineating BA. Approximately 5% of the BA detected by VIIRS-BA was not detected by the other products, which is up to 5 times more than the other products. It is worth noting that all the products only disagreed on 16% of the BA fraction surface.

4.2.2. Temporal distribution

Fig. 6c and d displays the monthly distribution of the VIIRS-BA output based on confidence levels. In this analysis, the BA value for each category represents the cumulative sum of the current category and all preceding categories. Notably, from the results shown in Fig. 6c and

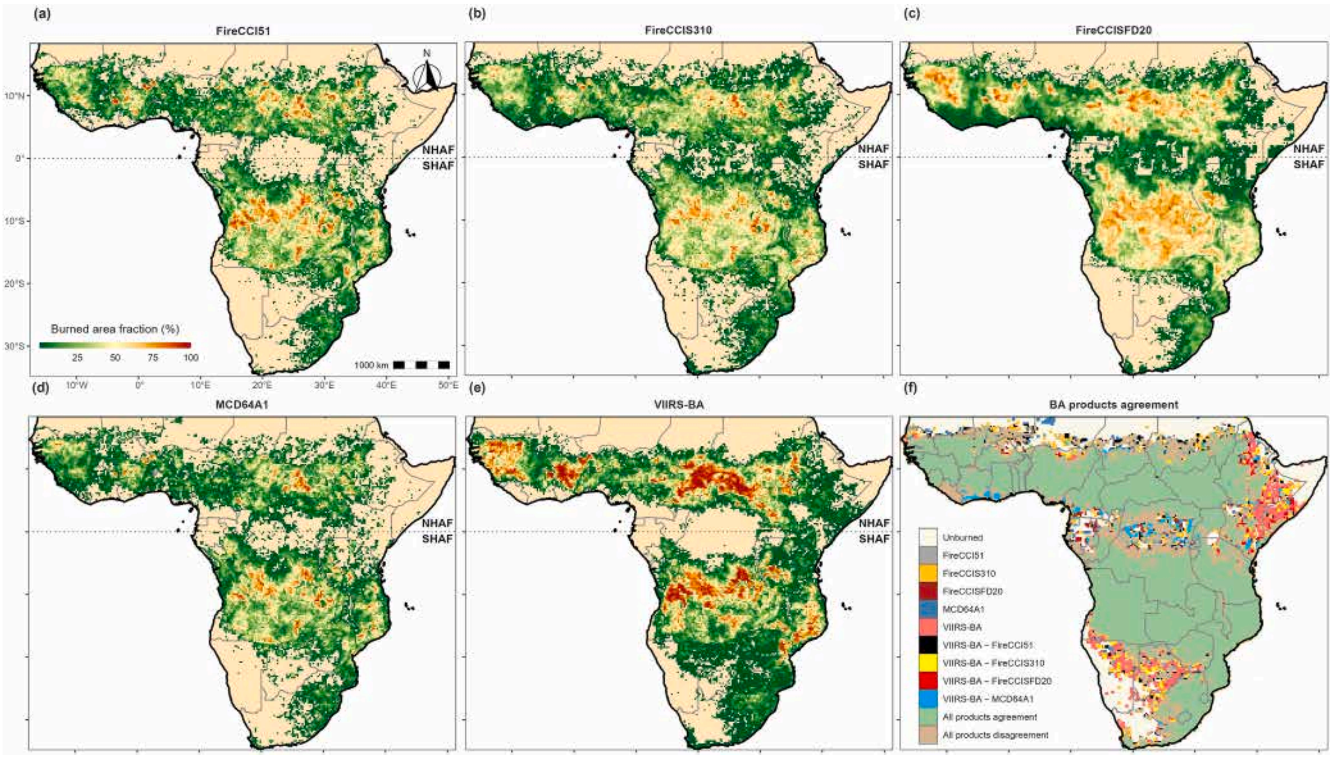

Fig. 7. Spatial distribution amongst burned area products at 0.25° cell grid resolution in the Northern and Southern African hemispheres (NHAF, SHAF, respectively) of Sub-Saharan Africa. (a) to (e): the burned area fraction by products; a) FireCCI51, b) FireCCIS310, c) FireCCISFD20, d) MCD64A1, e) VIIRS-BA. f) spatial agreement and discrepancy.

d, it is evident that the highest BA values are associated with low confidence, while the lowest values correspond to high confidence. To facilitate clearer and more straightforward comparisons, we intentionally focused on the moderate confidence product of VIIRS-BA M for the monthly comparisons with other BA products. In Fig. 8, this particular product is referred to as VIIRS-BA.

Both VIIRS-BA and the FireCCISFD20 product detected a larger amount of BA compared to the other three products throughout all months, particularly during periods with high fire occurrence (Fig. 8). The values for VIIRS-BA and the FireCCISFD20 product are quite similar, except for May and November when VIIRS-BA detected more BA than FireCCISFD20 in NHAF. On the other hand, in SHAF, FireCCISFD20 detected more BA than VIIRS-BA during September to November. Despite variations in magnitude, the monthly BA shows similar trends in terms of fluctuation for all BA product. The peak observed in May for VIIRS-BA in the NHAF, which indicates a potential anomaly, will be thoroughly addressed in section 3.4. Typically, the majority of fire occurrences takes place in NHAF during November to March, while in SHAF, they are more prevalent from June to September.

4.3. Spatial validation

4.3.1. Overall assessment

Our VIIRS-BA product demonstrates varying levels of accuracy depending on the confidence level considered (Table 5). The OA averages at 75.7% (minimum: 74.7%; maximum: 76.8%). The CE ranges from 7.8% to 23.4%, while the OE falls between 29.4% and 58.8%. The DC and JC reach 64.3% and 47.3%, respectively. The RelB ranges from 28.6% to 31.9%, indicating a positive bias throughout. The Kappa values indicate a fair to moderate level of agreement, ranging from 38.3% to 45.2%. In contrast, the F1 scores are higher, reaching up to 64.3%, which suggests a relatively good balance between precision and recall despite the moderate agreement.

In general, the four other products demonstrate good accuracies, with an OA ranging from 79.4% (MCD64A1) to 90.7% (FireCCISFD20). These products had relatively low CE (below 10%) with the lowest value

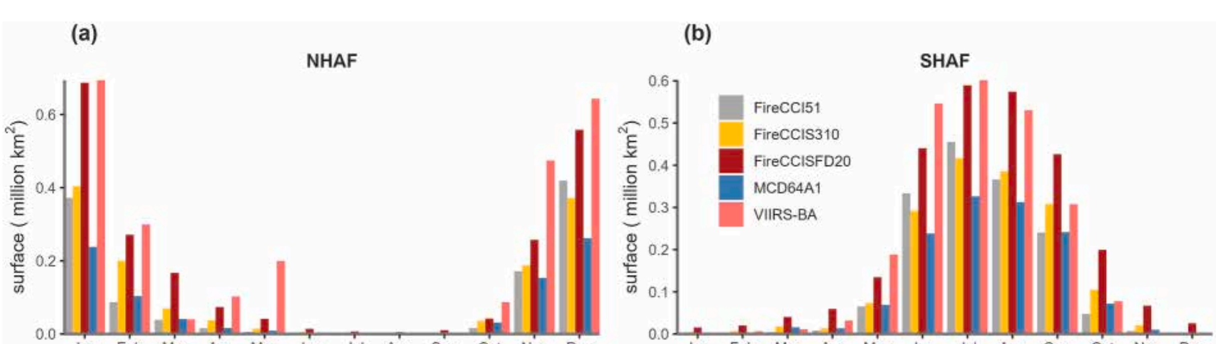

Fig. 8. Monthly distribution of burned area by zone (Northern and Southern African hemisphere) using FireCCI51, FireCCIS310, FireCCISFD20, MCD64A1 and VIIRS-BA products.

Table 5

Confusion matrix showing the overall comparison of classification accuracy of different burned area products over the 27 validation areas. The areas are given in square kilometers (km^2) while the error metrics are given in percentage (%). TP: true positive; FP: false positive; TN: true negative; FN: false negative; OA: overall accuracy; CE: commission error; OE: omission error; DC: Dice coefficient; JI: Jaccard index; RelB: Relative Bias; F1: F-score; Kappa: Cohen's Kappa. The values in bold represent the best metrics for each group: (1) Global/Regional and (2) VIIRS-BA products.

	TP	FP	TN	FN	OA	CE	OE	DC	JI	RelB	F1	Kappa
	(km^2)				(%)							
FireCCI51	108.3	36.5	363.6	82.0	79.9	9.1	43.1	64.6	47.8	23.7	64.6	51.0
FireCCIS310	112.8	31.7	368.4	77.5	81.5	7.9	40.7	67.4	50.8	21.4	67.4	54.8
FireCCISFD20	160.2	30.2	355.4	22.7	**90.7**	7.8	**12.4**	**85.8**	**75.2**	**11.3**	**85.8**	**78.9**
MCD64A1	94.3	25.8	374.3	96.0	79.4	**6.4**	50.5	60.8	43.6	24.0	60.8	47.7
VIIRS-BA L	134.4	93.6	306.5	55.9	74.7	23.4	**29.4**	**64.3**	**47.3**	31.9	**64.3**	44.9
VIIRS-BA M	110.4	57.0	343.1	80.0	**76.8**	14.2	42.0	61.7	44.6	**28.6**	61.7	**45.2**
VIIRS-BA H	79.9	31.3	368.9	110.5	76.0	**7.8**	58.8	53.0	36.0	29.3	53.3	38.3

for MCD64A1 (6.4%). For the remaining metrics, FireCCISFD20 outperformed the others, exhibiting the lowest OE of 12.4%, the highest DC of 85.8%, a JI of 75.2%, and a far better balance between precision and recall with F1 of 85.8%. In terms of RelB and Kappa, FireCCISFD20 demonstrated the closest agreement to the reference data with a positive RelB of 11.3%, whereas the others displayed a RelB exceeding 21%. Its Kappa percentage of 78.9% shows substantial agreement with the reference data.

Among the moderate spatial resolution products (excluding FireCCISFD20), the VIIRS-BA L product, characterized by a low confidence level, exhibits the lowest OE at 29.4%. On average, it is 44.8%, with a range of 40.7%–50.5%, for the other moderate spatial resolution products. In contrast, both VIIRS-BA M (moderate confidence) and VIIRS-BA H (high confidence) show values that are fairly similar to the others. Notably, VIIRS-BA L stands out with a value close to double that of the others.

4.3.2. Ecoregional assessment

Accurate measurement of BA is crucial for evaluating the impact of wildfires on the environment across all ecoregions. The "Tropical Savannas" biome showed the best accuracies for most metrics, except CE and RelB. For CE and RelB, the "Mediterranean Forest" and "Others" biomes had the highest accuracies across all products. In contrast, these two biomes had the lowest accuracies for the remaining metrics.

In the "Mediterranean Forest" biome, the OE is almost null for all products, while the CE is significantly greater than 95%. This results in high overall accuracy, exceeding 80% for all products. However, it is important to note that this value conceals the fact that both CE and OE are quite poor for all products. In the "Others" biome, we observed a similar trend. The VIIRS-L product has an OE below 40%, while other products have an OE above 80%. For the "Temperate Grasslands" and "Tropical Forest" biomes, the CE is low for almost all products. However, FireCCISFD20 outperforms others in terms of OE, followed by VIIRS-L. In the "Tropical Savannas" biome, FireCCISFD20 has the lowest OE, followed by VIIRS-L. For CE, MCD64A1 has the lowest value. Fig. 9 displays some example of BA results obtained from BARD using the four BA products.

4.4. Regional focus

The seasonal analysis of VIIRS-BA revealed a significant increase in BA during the month of May in the NHAF region. This increase appeared to be not previously observed when comparing the VIIRS-BA product, particularly the moderate confidence level, with other BA products in the NHAF region. Consequently, we focused in investigating the specific areas where these differences occurred. Fig. 10 illustrates an example of a small region located north of Guinea in West Africa, specifically examining the spatial comparison for the month of May.

Upon examination, it becomes evident that VIIRS-BA successfully detects a substantial portion of BA that the other products fail to capture. The spatial distribution is somewhat similar to that of FireCCISFD20, but with a higher density of BA patches, which could explain the differences in monthly BA. Notably, the patches appear more fragmented in FireCCISFD20 compared to VIIRS-BA. While this fragmentation trend is also

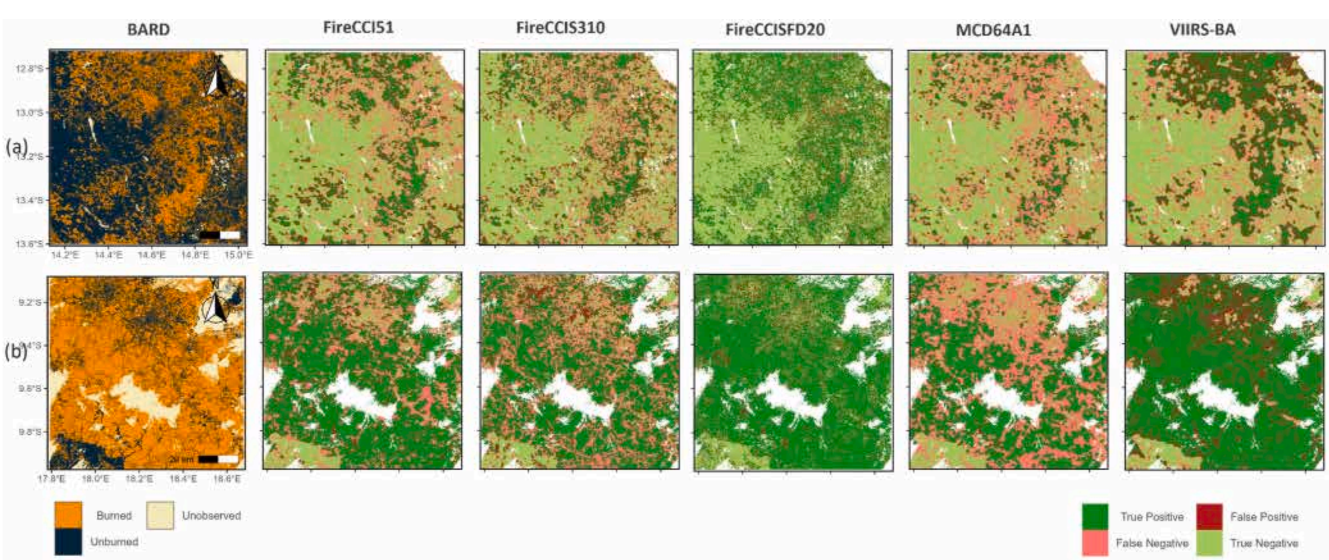

Fig. 9. Example of burned area results obtained from BARD and confusion maps with burned area products at four sites: (a) Sentinel-2 (S2) tile 33LVF, (b) S2 tile 33LZK. The main biome for site (a) is "Temperate Grasslands" and "Tropical Savannas" for site (b).

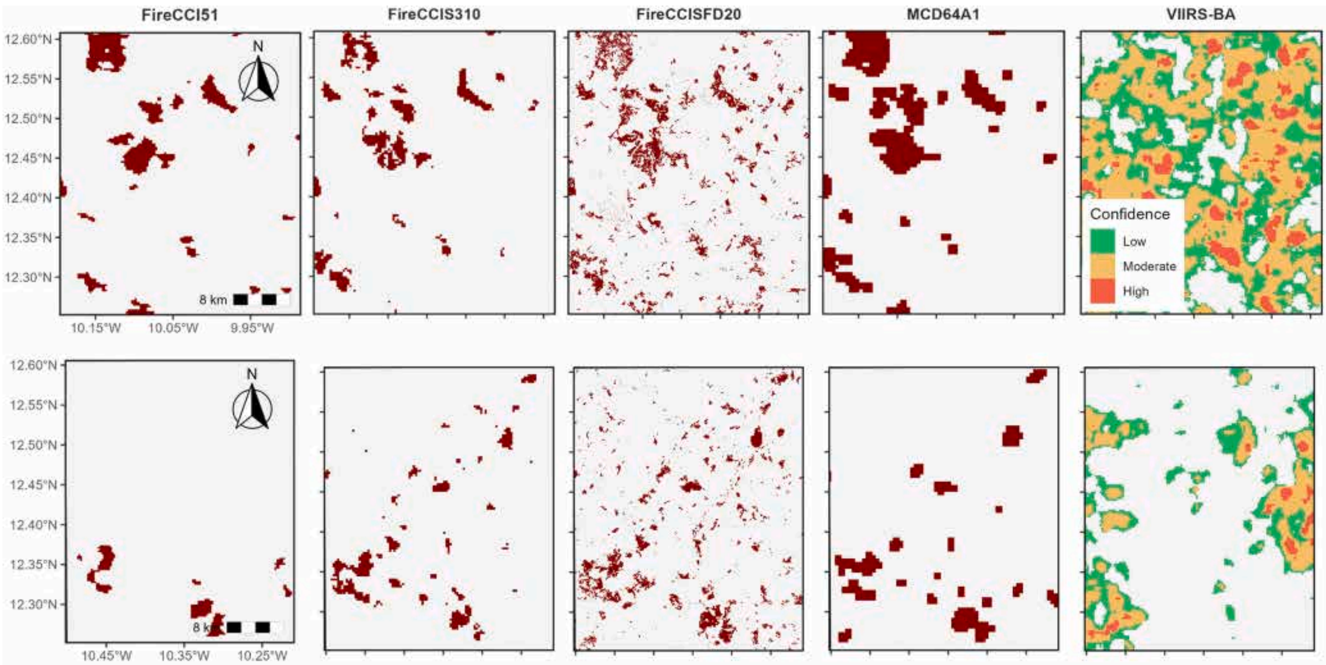

Fig. 10. Comparison of burned area products in May in northern Guinea, West Africa, highlighting disparities among the different products.

observed in the other three products, their lower spatial resolution makes them appear coarser than FireCCISFD20.

To further illustrate the general pattern of detected BA at a local scale, we compare the various BA products at their original spatial resolution for the year 2019 (Fig. 11). For this comparison, we selected two sample sites situated within the "Tropical savannas" biome, which covers 66% of the study area and experiences over 80% of fire occurrences (section 3.1). The first site (Fig. 11a) is located near Benin's Pendjari National Park in West Africa and consists of grasslands and croplands, according to the MODIS Land Use and Land Cover (LULC) data. The second site (Fig. 11b) is situated in eastern Zambia, South-Central Africa, and includes a mix of forests, savannas, and grasslands based on the MODIS LULC data.

In both sample sites, all BA products exhibit similar shapes, indicating significant BA. However, FireCCISFD20 and VIIRS-BA exhibit notably higher BA densities compared to the other products. Furthermore, fire patches identified by VIIRS-BA tend to be larger in size compared to the other products. Interestingly, both FireCCI51 and MCD64A1 products show a noticeable underestimation of the BA in both sample sites.

5. Discussion

5.1. Detection capabilities

The estimated BA for the year 2019 obtained from the VIIRS-BA product, at the lowest confidence threshold, was relatively similar to the FireCCISFD20 product, with values of 5.1 and 4.7 million km^2 respectively. In comparison, the FireCCIS310 estimate was slightly lower at 2.9 million km^2. When comparing the more recent BA products (VIIRS-BA and FireCCISFD20) to global products (FireCCI51, MCD64A1), it was found that the former tended to detect approximately twice as much BA. These findings confirm the results of Roteta et al. (2019) that previous moderate spatial resolution estimations of global

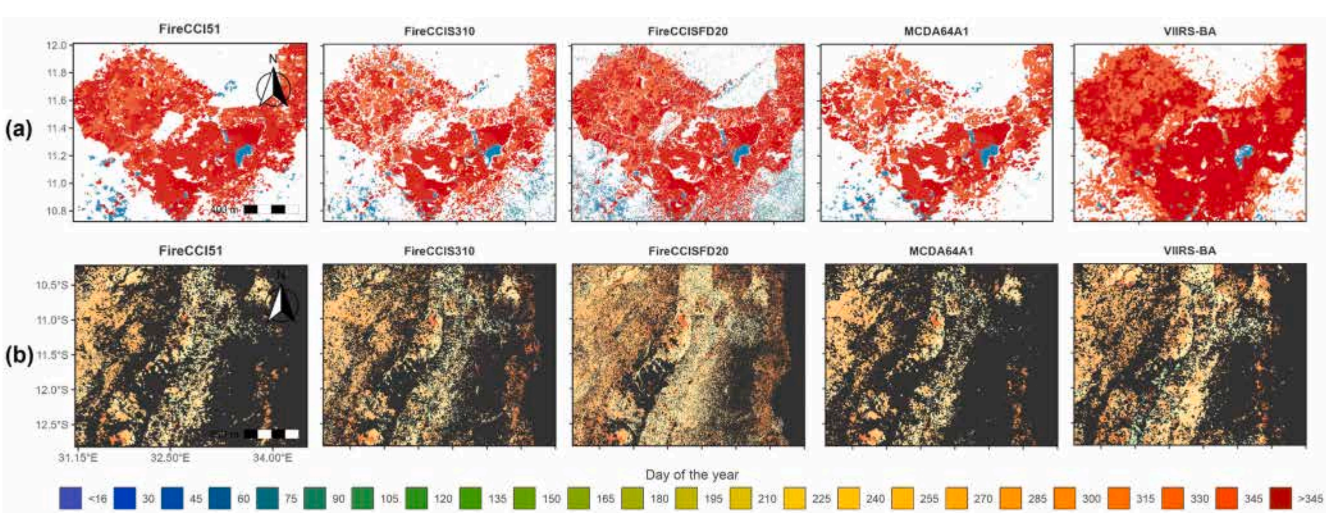

Fig. 11. Comparison of different burned area products at two subset sites in Africa; (a) Pendjari National Park in Benin, West Africa; (b) Eastern Zambia, South-Central Africa. The burned areas in 2019 are displayed based on their corresponding day of the year.

biomass burning may have underestimated BA in Africa. As a consequence, the effect of biomass burning on fire emissions could be significantly larger than what was previously reported (Ramo et al., 2021).

Two main factors could account for this discrepancy. Firstly, the disparity in observed results may stem from the differences in input resolution utilized by the algorithms. The use of moderate spatial resolution satellite imagery in the MODIS-based BA products (FireCCI51, MCD64A1) could result in the underrepresentation of small fires and incomplete depiction of larger fire extents (Hall et al., 2021; Xu et al., 2022a). Previous studies on accuracy assessments according to fire size actually concluded on the missing small fires and higher BA in large fires (Nogueira et al., 2017; Campagnolo et al., 2021). Conversely, products with higher spatial resolution, such as FireCCIS310, FireCCISFD20, and VIIRS-BA, which also employ VIIRS-AF input, exhibit enhanced sensitivity to smaller fires with lower intensity, as previously anticipated by Schroeder et al. (2014).

Secondly, the significant improvement in performance can be attributed to the reduction of OE in both FireCCISFD20 (20 m) and VIIRS-BA (250 m). These products utilize higher spatial resolution surface reflectance data in their algorithms, which surpasses the capabilities of FireCCIS310 (300 m). This enhancement allows for more accurate detection of smaller fire patches, leading to an overall improvement in the performance of these products. This capability correlates with the concept introduced by Boschetti et al. (2004) regarding the "low-resolution bias," which refers to the imprecision introduced by the difference in spatial resolution between high and low spatial resolution data. Our finding is consistent with Chuvieco et al. (2022), who also observed an increase in accuracy performance due to the higher temporal resolution of the combined S2 A and B missions. The combination of VIIRS-SR, our composite mode, and VIIRS-AF data at a 15-day interval effectively addresses the issue of burn scars that quickly disappear. This challenge is commonly observed in SSA, where there is a prevalence of low or moderate intensity fires with short durations. These fires are often a result of prescribed burning practices carried out early in the mild dry season for vegetation management (Teunissen et al., 2022), as well as the widespread use of "slash and burn" agricultural practices in the region (Bauer et al., 2019). These factors contribute to the generation of small fires, resulting in a mosaic-like pattern of burn patches with relatively low intensity. Although the pre and post-image approach may not be suitable for many small fires due to their short time duration (Hall et al., 2016), our utilization of the mentioned satellite data and technique allows us to better capture the highly dynamic fire regimes in SSA.

As a result, FireCCISFD20 and VIIRS-BA emerge as the most accurate products in terms of OE. The findings reveal a substantial reduction in OE with VIIRS-BA, presenting OE values between 58% and 68% lower than those of other global BA products. However, the regional product FireCCISFD20 demonstrates a 37% improvement in OE compared to VIIRS-BA. VIIRS-BA exhibits CE up to three times higher than the CE of other BA products. The observed superiority of FireCCISFD20 over the others is not unexpected. This anticipated disparity may be attributed to the fact that, in contrast to FireCCISFD20 with a 20 m resolution, each pixel of VIIRS-BA represents a 250 m $\times$ 250 m area. The validation data used also has a 20 m resolution, leading to higher CE in VIIRS-BA. Consequently, the total burned surface area estimated by VIIRS-BA is slightly higher than that of FireCCISFD20. In fact, one pixel identified as burned in VIIRS-BA covers approximately 150 times the area of a pixel in FireCCISFD20, highlighting an acknowledged edge effect in moderate spatial resolution BA detection (Humber et al., 2019). While improvements in pre-processing could potentially address this issue, a study by Franquesa et al. (2022) suggests that moderate spatial resolution sensors like VIIRS or MODIS may already be close to the maximum achievable CE.

VIIRS-BA offers two significant advantages over FireCCISFD20. Firstly, the main input data for VIIRS-BA has been consistently available for a longer period compared to FireCCISFD20. This is particularly beneficial for users who require long time-series data on BA (Mouillot et al., 2014). Generating long-term records necessitates the combination of products derived from different input datasets, and ensuring their consistency is crucial to avoid any disruptions in temporal trends (Lizundia-Loiola et al., 2021). Secondly, the processing time required to generate FireCCISFD20 for large areas presents two main challenges. Firstly, there is a large volume of input data that needs to be processed, which can be time-consuming. Additionally, the complexity of the time series analysis needed to detect BA adds to the processing time (Chuvieco et al., 2022). Although the S2 satellites provide a higher spatial resolution, the presence of a time gap of around 3–5 days between overpasses (excluding cloud cover) leads to relatively significant errors (Hall et al., 2021). The theoretical temporal resolution is likely to further decrease during the rainy season, thus challenging the consistent assessment over time.

5.2. Challenges and future directions

Some internal issues were identified in the VIIRS-SR, specifically in the Collection 1 used in this study (Giglio et al., 2019). One of the problems encountered is the presence of cloud mask artifacts, which can lead to higher CE along the edges of inland water bodies and at high latitudes. These artifacts may explain the unusually high BA values observed in May for NHAF and February for SHAF. To address this issue, in the current version of VIIRS-BA, we recommend utilizing either the moderate or high confidence products for specific time and spatial areas. It is advised to consider the associated per-pixel uncertainty layer, similar to the one used by the Fire_cci project (last accessed in June 2023). It is worth noting that the upcoming VIIRS-SR Collection 2 is expected to resolve this problem (Giglio et al., 2023).

Until the potential limitation mentioned above are addressed, the question regarding a potentially new insight into fire activity in SSA remains unresolved. VIIRS-BA, in particular, detected an extended fire season in the NHAF, with a notable increase in the detection frequency of late fires. However, the existence of any temporal shift or new pattern in BA in that region is yet to be determined.

In general, moderate to low spatial resolution BA products often encounter mixed pixel issues, where a single pixel may contain a blend of burned and unburned areas or different land cover types. This challenge is also relevant to our VIIRS-BA product, given its base spatial resolution of 250 m. However, most BA products with moderate to low spatial resolution, such as those used for comparing with our VIIRS-BA product in the literature, primarily differentiate between burned and unburned classes. Yet, the accuracy of final products can be enhanced with additional steps to reduce potential errors in estimating the actual extent of BA. Strategies to improve accuracy include integrating VIIRS data with higher resolution data (e.g., S2) through fusion approaches to enhance spatial detail, as demonstrated by studies such as those by Pinto et al. (2021) and Seydi et al. (2022) for forest fires in Europe. However, challenges remain regarding data continuity for long-term analysis, especially since S2 data are relatively recent and may not cover large regions like the SSA comprehensively. Additionally, handling high-resolution data can pose computational challenges. Another approach involves using statistical methods or machine learning techniques to model and compensate for mixed pixel effects in BA mapping, as exemplified by technologies like super-resolution burned-area mapping (SRBAM) (Wang et al., 2019). Similarly, the Burned-Area Subpixel Mapping (BASM) workflow has been designed to accurately identify BA within mixed pixels, benefiting post-fire management, carbon budget quantification, and other assessments (Xu et al., 2022b). However, these techniques are not infallible, as spectral confusion can still arise when distinguishing between BA and other land cover types within the same pixel (Liu et al., 2019).

In the future, an assessment of our VIIRS-BA can be conducted by comparing it with the planned NASA VIIRS Collection 2 VNP64A1 BA product (Giglio et al., 2023). The upcoming version of our VIIRS-BA will incorporate the NOAA-20 VIIRS-AF data, which has been available since 2020 (FIRMS, last accessed March 2023). This integration of active fire data from both Suomi NPP and NOAA-20 has the potential to further enhance the accuracy of VIIRS-BA.

5.3. Research contributions and potential impacts

The findings of this study underscore the significant impact of integrating VIIRS-SR and VIIRS-AF into BA mapping algorithms, benefiting not only the fire community but also various applications. The West African Science Service Centre on Climate Change and Adapted Land Use (WASCAL) plans to integrate this product (VIIRS-BA) into their climate and environmental services. This integration aims to provide harmonized and up-to-date information on BA in SSA addressing the current lack of such services in the region. The improved detection capabilities, along with enhanced spatial and temporal accuracies, have far-reaching implications. One notable implication is the utilization of higher spatial resolution data for obtaining more precise information on biomass burning patterns. This offers advantages such as easier and faster access to near real-time information compared to FireCCISFD20, despite FireCCISFD20 having a higher spatial resolution. This advancement holds particular importance in understanding the environmental consequences of biomass burning, identifying fire sources and causes (Ramo et al., 2021), enhancing fire monitoring and prediction (Chen et al., 2022), and guiding land use and fire management policies (Zhao et al., 2017).

6. Conclusion

As the MODIS mission is coming to an end, it is important to find suitable replacements to continue providing global maps of BA at a moderate level of detail in the future. The VIIRS instrument shows promise as a potential replacement for MODIS due to its enhanced capabilities. In this study, a new regional BA product called VIIRS-BA was introduced, which solely utilizes data from the VIIRS instrument, including VIIRS-SR and VIIRS-AF data. The current version of VIIRS-BA allows for the detection of burned scars at a resolution of 250 m and provides updates every 15 days. The product utilizes spectral indices before and after fires, as well as a RF image classification technique implemented in the GEE platform. The output of the product includes information presented at three confidence levels, indicating the reliability of the detected BA. To evaluate the performance of VIIRS-BA, comparisons were made with global BA products such as FireCCI51, FireCCIS310, and MCD64A1, as well as a regional product called FireCCISFD20. The accuracy of VIIRS-BA was also validated using an independent reference dataset of BA (BARD). This allowed for a comprehensive assessment of the reliability and effectiveness of the VIIRS-BA product in detecting and mapping BA.

This research emphasises the significance of improved detection capabilities in BA mapping. The VIIRS-BA product identified 5.1 million km^2 of BA in SSA for the year 2019, significantly exceeding the BA detected by other global moderate spatial resolution products and closely aligning with the fine resolution FireCCISFD20 product, with only a 7.3% difference. The comparison of different BA products highlights the underestimation of global biomass burning in previous estimations. Factors contributing to this discrepancy include variations in resolution of reflectance products input, with higher spatial resolution products exhibiting enhanced sensitivity to smaller fires. The reduction of OE in FireCCISFD20 and VIIRS-BA, achieved through the use of higher spatial surface reflectance data, improves overall performance. The differences in BA detection were less pronounced in biomes with persistent biomass burning, such as “Tropical Savannas” and “Temperate Grasslands,” suggesting that the VIIRS-BA product is particularly effective in these regions. Despite some commission problems in VIIRS-BA due to its lower spatial resolution, it offers advantages in terms of longer data availability and faster processing time. Integrating VIIRS-SR and VIIRS-AF data enhances environmental assessments, fire monitoring, and land use policies. Future directions involve improving the overall accuracy and reliability of the VIIRS-BA product. The upcoming BA products and integrating additional active fire data from NOAA to further enhance accuracy (reduce CE) and enable more precise information on biomass burning patterns and their consequences.

CRediT authorship contribution statement

Boris Ouattara: Writing – original draft, Validation, Methodology, Data curation, Conceptualization. **Michael Thiel:** Writing – review & editing, Supervision, Resources, Project administration, Funding acquisition. **Barbara Sponholz:** Writing – review & editing, Supervision, Funding acquisition. **Heiko Paeth:** Writing – review & editing, Supervision, Funding acquisition. **Marta Yebra:** Writing – review & editing, Conceptualization. **Florent Mouillot:** Writing – review & editing, Conceptualization. **Patrick Kacic:** Writing – review & editing. **Kwame Hackman:** Writing – review & editing, Data curation, Conceptualization.

Declaration of competing interest

The authors declare the following financial interests/personal relationships which may be considered as potential competing interests:

Boris Ouattara reports financial support was provided by Federal Ministry of Education and Research Bonn Office. Michael Thiel reports financial support was provided by Federal Ministry of Education and Research Bonn Office. If there are other authors, they declare that they have no known competing financial interests or personal relationships that could have appeared to influence the work reported in this paper.

Data availability

Data will be made available on request.

Appendix

A1. Experiment to test the influence of spatial resolution on burned area (BA) accuracy and scars detection capabilities

Introduction

New research indicates that small fires are frequently overlooked in estimating burned areas (BA), potentially leading to bias (Randerson et al., 2012; Roteta et al., 2019; Ramo et al., 2021). The pronounced heterogeneity of Africa’s land use/land cover (LULC) makes precise BA classification difficult (Linderman et al., 2005; Adole et al., 2018).

We assessed the impact of spatial resolution on BA products using the dataset outlined in Section 2.2 of the main document. We wanted to find the 250 m, 375 m, or 500 m spatial resolutions that best match the BA patterns seen in high-resolution Sentinel-2 (S2) data from the Burned Area Reference Database (BARD). These resolutions should also be able to capture the different burn scar patterns that are common in African mosaic burning regimes (Laris, 2005).

We selected seven validation sites covering the Northern African hemisphere (NHAF) from the BARD dataset (Stroppiana et al., 2022), as depicted in Fig. A.1. Section 2.4.2 of the main document provides BARD details. Accuracy was evaluated using Congalton's (2001) error matrix methodology, and metrics such as omission and commission error (OE, CE), Dice coefficient (DC), Jaccard Index (JI), and Relative Bias (RelB) were calculated.

To assess heterogeneity levels, we used fire patch size distribution as a fragmentation metric. Boschetti et al. (2004) identified this landscape metric as influencing the accuracy of moderate-to low-resolution maps. Pixel-level information obtained at the three spatial resolutions mentioned (250 m, 375 m, and 500 m) derived fire patch identification.

Fig. A.1. Study area for the test representing the Northern African hemisphere (NHAF) according to the GFED regionalization (Van Der Werf et al., 2017) and the seven validation areas. These areas were based on a window size of 100 × 100 km, located at the center of the Sentinel-2 tile. The biome is Tropical Savannas. 1: 29PLP; 2: 29PLM; 3: 34PDU; 4:34NCP; 5: 35PRN; 6: 35PQM; 7: 36PYU.

Accuracy assessment

For all confidence levels, the 250 m spatial resolution demonstrates the highest accuracy except for CE, although the difference compared to 375 m and 500 m is not very significant (Table A.1). Given the inverse relationship between OE and CE, we expected this slightly higher CE.

Table A.1
Confusion matrix showing the overall comparison of classification accuracy of VIIRS-BA at the different confidence and spatial resolution over the seven validations area. The areas are given in square kilometers (km^2) while the error metrics are given in percentage (%). TP: true positive; FP: false positive; TN: true negative; FN: false negative; OA: overall accuracy; CE: commission error; OE: omission error; DC: Dice coefficient; JI: Jaccard index; RelB: Relative Bias. The values in bold represent the best metrics for each group: (1) Low confidence; (2) Moderate confidence; (3) High confidence.

Confidence	Spatial resolution	TP	FP	TN	FN	OA	CE	OE	DC	JI	RelB
		(km^2)				(%)					
Low	250	21.4	25.7	16.1	7.7	52.9	61.5	**26.5**	**56.2**	**39.1**	**53.6**
	375	20.9	25.5	16.3	8.2	52.5	61	28.2	55.4	38.3	54.2
	500	20.6	25.3	16.5	8.5	52.4	**60.5**	29.2	55	37.9	54.5
Moderate	250	17.0	19.8	22.0	12.2	54.9	47.4	**41.8**	**51.5**	**34.7**	**54.2**
	375	16.0	19.3	22.4	13.2	54.1	46.3	45.2	49.5	32.9	55.7
	500	15.3	18.8	23.0	13.9	53.9	**45**	47.7	48.2	31.8	56.6
High	250	10.8	11.6	30.1	18.4	57.6	27.9	**63.1**	**41.7**	**26.4**	**55.6**
	375	9.9	11.0	30.7	19.3	57.3	26.4	66.1	39.5	24.6	57
	500	9.3	10.6	31.2	19.8	57.1	**25.4**	67.9	38.1	23.5	57.7

Fire patch size

The analysis of burned area (BA) patches in this study revealed insights into their size distribution and occurrence (Fig. A.2). These patches were identified every 2 weeks (15 days) and categorized into four size classes: >250 ha, 125–250 ha, 25–125 ha, and <25 ha.

Across all confidence levels, the distribution of patch size categories was quite similar, except for the 125–250 ha category, which had a ratio almost two times lower than the others. However, the VIIRS-BA at 250 m detected more burned occurrences than others, up to two to three times for the smallest category (<25 ha).

Based on this 15-day categorization, small fires (<125 ha) accounted for 40.9% (500 m) to 57.5% (250 m) of the total burned area in the NHAF region (Table A.2), consistent with findings from Ramo et al. (2021) in Africa.

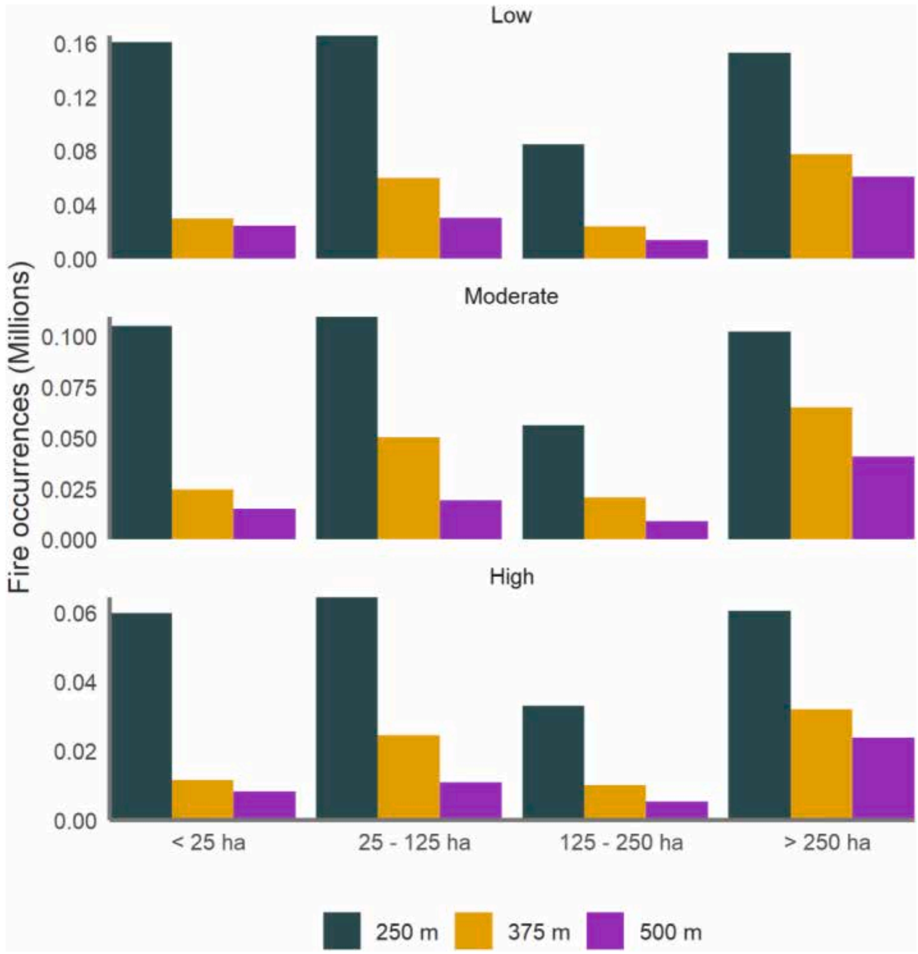

Fig. A.2. Total burned areas according to the patch size occurrence distribution.

Table A.2
Average patch size distribution (%) according to VIIRS-BA spatial resolution. Standard deviation is indicated in parentheses.

Spatial resolution	Patch size			
	<25 ha	25–125 ha	125–250 ha	>250 ha
250 m	28.1 (0.5)	29.4 (0.1)	15.1 (0.1)	27.4 (0.3)
375 m	15.3 (0.4)	31.3 (0.1)	12.7 (0.3)	40.7 (0.2)
500 m	18.0 (0.9)	22.9 (0.4)	10.8 (0.3)	48.4 (1.1)

Conclusion

Boschetti et al. (2004) investigated the impact of low spatial resolution on BA product accuracy, highlighting the difficulty of accurately classifying pixels in low-resolution datasets. They termed this phenomenon "low-resolution bias," which refers to inaccuracies arising from differences in spatial resolution between high and low spatial resolution datasets. Laris and Wardell (2006) further addressed this issue, noting that coarse spatial resolution data often struggle to detect small BA accurately, resulting in an underestimation of BA extent, especially in areas with fragmented burn patterns.

Our analysis revealed a notable occurrence of small BA patches (<25 ha), indicating a highly fragmented and heterogeneous study area. This fragmentation poses challenges for accurate BA detection, particularly with lower spatial resolutions (375 m, 500 m). Additionally, our findings align with those of Smith et al. (2003), who observed that classification accuracy tends to decrease as patch size decreases and LULC diversity increases.

Based on the accuracy assessment and patch size distribution results, we selected a spatial resolution of 250 m for our final VIIRS-BA product. This resolution offers a balance between detecting small BA patches and accurately capturing the heterogeneity of the landscape.

A2. Variable importance

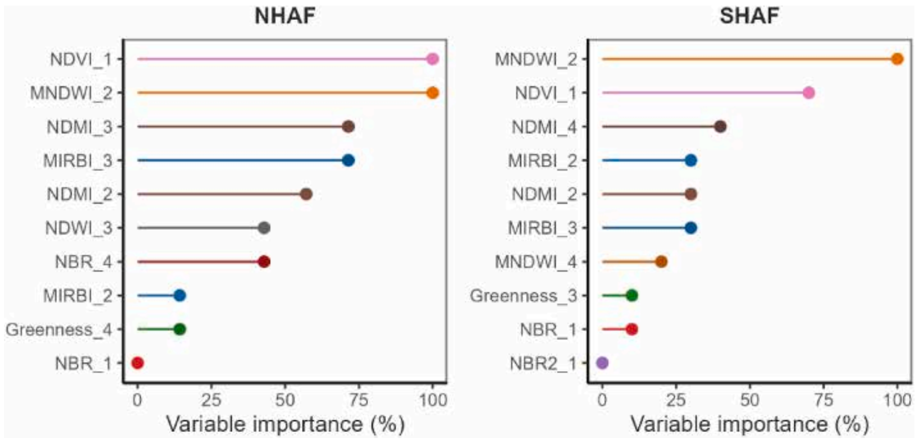

Fig. A.3. The ten most important features of the random forest in the Northern and Southern African hemispheres (NHAF and SHAF, respectively). The segment length indicates, in percentage, the importance of the 24 model runs, which correspond to each biweekly output for each region (NHAF and SHAF). Numbers correspond to the derivatives of the original index explained in Section 2.3.2 of the main document. These numbers correspond to: 1) pre-fire index; 2) post-fire index; 3) differenced normalized index; 4) relativised index.

References

Abdikan, S., Bayik, C., Sekertekin, A., Bektas Balcik, F., Karimzadeh, S., Matsuoka, M., Balik Sanli, F., 2022. Burned area detection using multi-sensor SAR, optical, and thermal data in mediterranean pine forest. Forests 13 (2), 347. https://doi.org/10.3390/f13020347.

Akagi, S.K., Yokelson, R.J., Wiedinmyer, C., Alvarado, M.J., Reid, J.S., Karl, T., Crounse, J.D., Wennberg, P.O., 2011. Emission factors for open and domestic biomass burning for use in atmospheric models. Atmos. Chem. Phys. 11 (9), 4039–4072. https://doi.org/10.5194/acp-11-4039-2011.

Ali, M., Dirawan, G.D., Hasim, A.H., Abidin, Muh R., 2019. Detection of changes in surface water bodies urban area with NDWI and MNDWI methods. Int. J. Adv. Sci. Eng. Inf. Technol. https://doi.org/10.18517/ijaseit.9.3.8692.

Al-Maliki, S., Ibrahim, T.I.M., Jakab, G., Masoudi, M., Makki, Jamal S., Vekerdy, Z., 2022. An approach for monitoring and classifying marshlands using multispectral remote sensing imagery in arid and semi-arid regions. Water 14 (10), 1523. https://doi.org/10.3390/w14101523.

Andela, N., Morton, D.C., Giglio, L., Yang, C., Werf, G.R.v. d., Kasibhatla, P.S., et al., 2017. A human-driven decline in global burned area. Science 356 (6345), 1356–1362. https://doi.org/10.1126/science.aal4108.

Bauer, S.E., Im, U., Mezuman, K., Gao, C.Y., 2019. Desert dust, industrialization, and agricultural fires: health impacts of outdoor air pollution in africa. J. Geophys. Res. Atmos. https://doi.org/10.1029/2018jd029336.

Belenguer-Plomer, M.A., Tanase, M.A., Chuvieco, E., Bovolo, F., 2021. CNN-based burned area mapping using radar and optical data. Rem. Sens. Environ. 260, 112468. https://doi.org/10.1016/j.rse.2021.112468.

Boschetti, L., Flasse, S., Brivio, P., 2004. Analysis of the conflict between omission and commission in low spatial resolution dichotomic thematic products: the pareto boundary. Rem. Sens. Environ. 91 (3–4), 280–292. https://doi.org/10.1016/j.rse.2004.02.015.

Boschetti, L., Roy, D.P., Giglio, L., Huang, H., Zubkova, M., Humber, M.L., 2019. Global validation of the collection 6 MODIS burned area product. Rem. Sens. Environ. 235, 111490. https://doi.org/10.1016/j.rse.2019.111490.

Bowman, D.M.J.S., Williamson, G.J., Abatzoglou, J.T., Kolden, C.A., Cochrane, M.A., Smith, A.M.S., 2017. Human exposure and sensitivity to globally extreme wildfire events. Nature Ecology & Evolution 1 (3), 58. https://doi.org/10.1038/s41559-016-0058.

Breiman, L., 2001. Random forests. Mach. Learn. 45 (1), 5–32. https://doi.org/10.1023/A:1010933404324.

Campagnolo, M.L., Libonati, R., Rodrigues, J.A.S., Pereira, J.M.C., 2021. A comprehensive characterization of MODIS daily burned area mapping accuracy across fire sizes in tropical savannas. In: Remote Sensing of Environment. https://doi.org/10.1016/j.rse.2020.112115.

Chen, J., Zheng, W., Shan, T., 2022. Dynamic fire monitoring analysis and risk assessment based on multisource satellite remote sensing. In: Mobile Information Systems. https://doi.org/10.1155/2022/5039644.

Chen, Y., Hou, J., Huang, C., Zhang, Y., Li, X., 2021. Mapping maize area in heterogeneous agricultural landscape with multi-temporal sentinel-1 and sentinel-2 images based on random forest. Rem. Sens. https://doi.org/10.3390/rs13152988.

Chuvieco, E., Lizundia-Loiola, J., Pettinari, M.L., Ramo, R., Padilla, M., Tansey, K., Mouillot, F., Laurent, P., Storm, T., Heil, A., Plummer, S., 2018. Generation and analysis of a new global burned area product based on MODIS 250 m reflectance bands and thermal anomalies. Earth Syst. Sci. Data 10 (4), 2015–2031. https://doi.org/10.5194/essd-10-2015-2018.

Chuvieco, E., Mouillot, F., van der Werf, G.R., San Miguel, J., Tanasse, M., Koutsias, N., García, M., Yebra, M., Padilla, M., Gitas, I., Heil, A., Hawbaker, T.J., Giglio, L., 2019. Historical background and current developments for mapping burned area from satellite Earth observation. Rem. Sens. Environ. 225 (March), 45–64. https://doi.org/10.1016/j.rse.2019.02.013.

Chuvieco, E., Roteta, E., Sali, M., Stroppiana, D., Boettcher, M., Kirches, G., Storm, T., Khairoun, A., Pettinari, M.L., Franquesa, M., Albergel, C., 2022. Building a small fire database for Sub-Saharan Africa from Sentinel-2 high-resolution images. Sci. Total Environ. 845. https://doi.org/10.1016/j.scitotenv.2022.157139.

Chuvieco, E., Yebra, M., Martino, S., Thonicke, K., Gómez-Giménez, M., San-Miguel, J., Oom, D., Velea, R., Mouillot, F., Molina, J.R., Miranda, A.I., Lopes, D., Salis, M., Bugaric, M., Sofiev, M., Kadantsev, E., Gitas, I.Z., Stavrakoudis, D., Eftychidis, G., et al., 2023. Towards an integrated approach to wildfire risk assessment: when, where, what and how may the landscapes burn. Fire 6 (5). https://doi.org/10.3390/fire6050215.

Congalton, R.G., 2001. Accuracy assessment and validation of remotely sensed and other spatial information. Int. J. Wildland Fire 10 (4), 321. https://doi.org/10.1071/WF01031.

Csiszar, I., Schroeder, W., Giglio, L., Ellicott, E., Vadrevu, K.P., Justice, C.O., Wind, B., 2014. Active fires from the Suomi NPP visible infrared imaging radiometer suite: product status and first evaluation results. J. Geophys. Res. Atmos. 119 (2), 803–816. https://doi.org/10.1002/2013JD020453.

Daldegan, G.A., Roberts, D.A., Ribeiro, F. de F., 2019. Spectral mixture analysis in Google Earth Engine to model and delineate fire scars over a large extent and a long time-series in a rainforest-savanna transition zone. Rem. Sens. Environ. 232, 111340. https://doi.org/10.1016/j.rse.2019.111340.

Fattore, C., Abate, N., Faridani, F., Masini, N., Lasaponara, R., 2021. Google earth engine as multi-sensor open-source tool for supporting the preservation of archaeological areas: the case study of flood and fire mapping in metaponto, Italy. Sensors. https://doi.org/10.3390/s21051791.

Fernández-Manso, A., Quintano, C., 2020. A synergetic approach to burned area mapping using maximum entropy modeling trained with hyperspectral data and VIIRS hotspots. Rem. Sens. 12 (5), 858. https://doi.org/10.3390/rs12050858.

Filipponi, F., 2019. Exploitation of sentinel-2 time series to map burned areas at the national level: a case study on the 2017 Italy wildfires. Rem. Sens. https://doi.org/10.3390/rs11060622.

FIRMS. (n.d.). Providing Active Fire Data for Near-Real Time Monitoring and Applications. Retrieved March 19, 2023, from https://firms.modaps.eosdis.nasa.gov/ .

Franquesa, M., Lizundia-Loiola, J., Stehman, S.V., Chuvieco, E., 2022. Using long temporal reference units to assess the spatial accuracy of global satellite-derived burned area products. In: Remote Sensing of Environment. https://doi.org/10.1016/j.rse.2021.112823.

Franquesa, M., Vanderhoof, M.K., Stavrakoudis, D., Gitas, I.Z., Roteta, E., Padilla, M., Chuvieco, E., 2020. Development of a standard database of reference sites for validating global burned area products. Earth Syst. Sci. Data 12 (4), 3229–3246. https://doi.org/10.5194/essd-12-3229-2020.

Frappart, F., Biancamaria, S., Normandin, C., Blarel, F., Bourrel, L., Aumont, M., Azemar, P., Vu, P.-L., Le Toan, T., Lubac, B., Darrozes, J., 2018. Influence of recent climatic events on the surface water storage of the Tonle Sap Lake. Sci. Total Environ. 636, 1520–1533. https://doi.org/10.1016/j.scitotenv.2018.04.326.

Friedl, Mark, Sulla-Menashe, D., 2022. MODIS/Terra+Aqua Land Cover Type Yearly L3 Global 500m SIN Grid V061 [Data set]. NASA EOSDIS Land Processes DAAC. https://doi.org/10.5067/MODIS/MCD12Q1.061.

Frost, G.V., Loehman, R.A., Saperstein, L.B., Macander, M.J., Nelson, P.R., Paradis, D.P., Natali, S.M., 2020. Multi-decadal patterns of vegetation succession after tundra fire on the Yukon-Kuskokwim Delta, Alaska. Environ. Res. Lett. 15 (2), 025003. https://doi.org/10.1088/1748-9326/ab5f49.

Gao, B., 1996. NDWI—a normalized difference water index for remote sensing of vegetation liquid water from space. Rem. Sens. Environ. 58 (3), 257–266. https://doi.org/10.1016/S0034-4257(96)00067-3.

GCOS, 2016. THE GLOBAL OBSERVING SYSTEM FOR CLIMATE: IMPLEMENTATION NEEDS GCOS-200. *GOOS-214)*.

Giglio, L., Boschetti, L., Roy, D., Humber, M., Hall, J., 2019. Collection 1 VIIRS Burned Area: Product User's Guide Version 1.0.

Giglio, L., Boschetti, L., Roy, D., Humber, M., Hall, J., Argueta, F., 2023. Collection 2 VIIRS Burned Area: Product User's Guide Version 1.0.

Giglio, L., Boschetti, L., Roy, D.P., Humber, M.L., Justice, C.O., 2018. The Collection 6 MODIS burned area mapping algorithm and product. Rem. Sens. Environ. 217 (August), 72–85. https://doi.org/10.1016/j.rse.2018.08.005.

Giglio, L., Randerson, J.T., van der Werf, G.R., 2013. Analysis of daily, monthly, and annual burned area using the fourth-generation global fire emissions database (GFED4). J. Geophys. Res.: Biogeosciences 118 (1), 317–328. https://doi.org/10.1002/jgrg.20042.

Google Developers, 2024. Projections in google earth engine. Retrieved March 1, 2024, from. https://developers.google.com/earth-engine/guides/projections.

Gorelick, N., Hancher, M., Dixon, M., Ilyushchenko, S., Thau, D., Moore, R., 2017. Google earth engine: planetary-scale geospatial analysis for everyone. Rem. Sens. Environ. 202, 18–27. https://doi.org/10.1016/j.rse.2017.06.031.

Grégoire, J.-C., Eva, H., Belward, A., Palumbo, I., Simonetti, D., Brink, A., 2013. Effect of land-cover change on africa's burnt area. Int. J. Wildland Fire. https://doi.org/10.1071/wf11142.

GTOS, 2009. Ecv T13 - fire disturbance. In: Assessment of the Status of the Development of the Standards for the Terrestrial Essential Climate Variables *(Version 27)*. http://www.fao.org/gtos/doc/ECVs/T13/T13.pdf.

Haas, O., Prentice, I.C., Harrison, S.P., 2022. Global environmental controls on wildfire burnt area, size, and intensity. Environ. Res. Lett. 17 (6). https://doi.org/10.1088/1748-9326/ac6a69.

Haliuc, A., Daniau, A.-L., Mouillot, F., Chen, W., Leys, B., David, V., Hanquiez, V., Dennielou, B., Schefuß, E., Bayon, G., Crosta, X., 2023. Microscopic charcoals in ocean sediments off africa track past fire intensity from the continent. In: Communications Earth & Environment. https://doi.org/10.1038/s43247-023-00800-x.

Hall, J.V., Argueta, F., Giglio, L., 2021. Validation of McD64a1 and FireCCI51 cropland burned area mapping in Ukraine. Int. J. Appl. Earth Obs. Geoinf. https://doi.org/10.1016/j.jag.2021.102443.

Hall, J.V., Loboda, T.V., Giglio, L., McCarty, G.W., 2016. A MODIS-based burned area assessment for Russian croplands: mapping requirements and challenges. In: Remote Sensing of Environment. https://doi.org/10.1016/j.rse.2016.07.022.

Hansen, M.C., Defries, R.S., Townshend, J.R.G., Sohlberg, R., 2000. Global land cover classification at 1 km spatial resolution using a classification tree approach. Int. J. Rem. Sens. 21 (6–7), 1331–1364. https://doi.org/10.1080/014311600210209.

Hantson, S., Arneth, A., Harrison, S.P., Kelley, D.I., Prentice, I.C., Rabin, S.S., Archibald, S., Mouillot, F., Arnold, S.R., Artaxo, P., Bachelet, D., Ciais, P., Forrest, M., Friedlingstein, P., Hickler, T., Kaplan, J.O., Kloster, S., Knorr, W., Lasslop, G., et al., 2016. The status and challenge of global fire modelling. Biogeosciences 13 (11), 3359–3375. https://doi.org/10.5194/bg-13-3359-2016.

Hardtke, L.A., Blanco, P.D., Valle, H. F. del, Metternicht, G., Sione, W.F., 2015. Semi-automated mapping of burned areas in semi-arid ecosystems using MODIS time-series imagery. Int. J. Appl. Earth Obs. Geoinf. https://doi.org/10.1016/j.jag.2014.11.011.

Honeck, E., Castello, R., Chatenoux, B., Richard, J.-P., Lehmann, A., Giuliani, G., 2018. From a vegetation index to a sustainable development goal indicator: forest trend monitoring using three decades of earth observations across Switzerland. ISPRS Int. J. Geo-Inf. 7 (12), 455. https://doi.org/10.3390/ijgi7120455.

Hu, X., Ban, Y., Nascetti, A., 2021. Uni-temporal multispectral imagery for burned area mapping with deep learning. Rem. Sens. https://doi.org/10.3390/rs13081509.

Humber, M.L., Boschetti, L., Giglio, L., Justice, C.O., 2019. Spatial and temporal intercomparison of four global burned area products. International Journal of Digital Earth. https://doi.org/10.1080/17538947.2018.1433727.

Justice, C.O., Román, M.O., Csiszar, I., Vermote, E.F., Wolfe, R.E., Hook, S.J., Friedl, M., Wang, Z., Schaaf, C.B., Miura, T., Tschudi, M., Riggs, G., Hall, D.K., Lyapustin, A.I., Devadiga, S., Davidson, C., Masuoka, E.J., 2013. Land and cryosphere products from Suomi NPP VIIRS: overview and status. J. Geophys. Res. Atmos. 118 (17), 9753–9765. https://doi.org/10.1002/jgrd.50771.

Kaiser, J.W., Heil, A., Andreae, M.O., Benedetti, A., Chubarova, N., Jones, L., Morcrette, J.-J., Razinger, M., Schultz, M.G., Suttie, M., van der Werf, G.R., 2012. Biomass burning emissions estimated with a global fire assimilation system based on observed fire radiative power. Biogeosciences 9 (1), 527–554. https://doi.org/10.5194/bg-9-527-2012.

Kauth, R.J., Thomas, G.S.P., 1976. The Tasselled Cap - A Graphic Description of the Spectral-Temporal Development of Agricultural Crops as Seen by Landsat.

Key, C., Benson, N., 1999. Measuring and remote sensing of burn severity: the CBI and NBR. In: Neuenschwander, L., Ryan, K. (Eds.), Joint Fire Science Conference and Workshop, vol. II. In: http://jfsp.nifc.gov/conferenceproc/index.htm.

Key, C.H., Benson, N.C., 2006. LA-1 Landscape Assessment (LA) Sampling and Analysis Methods.

Kumar, A., Kumar, A., Kumar, M., Bhat, J.A., 2022. Editorial: greenhouse gas emissions and terrestrial ecosystems. Front. Environ. Sci. 10. https://doi.org/10.3389/fenvs.2022.834444.

Lasko, K., 2019. Incorporating Sentinel-1 SAR imagery with the MODIS MCD64A1 burned area product to improve burn date estimates and reduce burn date uncertainty in wildland fire mapping. Geocarto Int. 0 (0), 1–21. https://doi.org/10.1080/10106049.2019.1608592.

Lewis, S.L., Edwards, D.P., Galbraith, D., 2015. Increasing human dominance of tropical forests. Science 349 (6250), 827–832. https://doi.org/10.1126/science.aaa9932.

Li, F., Zhang, X., Kondragunta, S., 2020. Biomass burning in africa: an investigation of fire radiative power missed by MODIS using the 375 m VIIRS active fire product. Rem. Sens. 12 (10), 1561. https://doi.org/10.3390/rs12101561.

Li, F., Zhang, X., Kondragunta, S., Csiszar, I., 2018. Comparison of fire radiative power estimates from VIIRS and MODIS observations. J. Geophys. Res. Atmos. 123 (9), 4545–4563. https://doi.org/10.1029/2017JD027823.

Liu, T., Marlier, M.E., Karambelas, A., Jain, M., Singh, S., Singh, M.K., Gautam, R., DeFries, R.S., 2019a. Missing emissions from post-monsoon agricultural fires in northwestern India: regional limitations of MODIS burned area and active fire products. Environmental Research Communications 1 (1), 011007. https://doi.org/10.1088/2515-7620/ab056c.

Liu, W., Zeng, Y., Li, S., Pi, X., Huang, W., 2019b. An improved spatiotemporal fusion approach based on multiple endmember spectral mixture analysis. Sensors 19 (11), 2443. https://doi.org/10.3390/s19112443.

Lizundia-Loiola, J., Franquesa, M., Boettcher, M., Kirches, G., Pettinari, M.L., Chuvieco, E., 2021. Implementation of the burned area component of the Copernicus climate change service: from MODIS to OLCI data. Rem. Sens. https://doi.org/10.3390/rs13214295.

Lizundia-Loiola, J., Franquesa, M., Khairoun, A., Chuvieco, E., 2022. Global burned area mapping from Sentinel-3 Synergy and VIIRS active fires. Rem. Sens. Environ. 282. https://doi.org/10.1016/j.rse.2022.113298.

Lizundia-Loiola, J., Otón, G., Ramo, R., Chuvieco, E., 2020. A spatio-temporal active-fire clustering approach for global burned area mapping at 250 m from MODIS data. Rem. Sens. Environ. 236, 111493. https://doi.org/10.1016/j.rse.2019.111493.

Long, T., Zhang, Z., He, G., Jiao, W., Tang, C., Wu, B., Zhang, X., Wang, G., Yin, R., 2019. 30m resolution global annual burned area mapping based on landsat images and Google Earth Engine. Rem. Sens. 11 (5), 1–30. https://doi.org/10.3390/rs11050489.

Mashhadi, N., Alganci, U., 2021. Determination of forest burn scar and burn severity from free satellite images: a comparative evaluation of spectral indices and machine learning classifiers. Int. J. Electron. Govern. https://doi.org/10.30897/ijegeo.879669.

McFeeters, S.K., 1996. The use of the Normalized Difference Water Index (NDWI) in the delineation of open water features. Int. J. Rem. Sens. 17 (7), 1425–1432. https://doi.org/10.1080/01431169608948714.

Moreno, M., Mouillot, F., 2021. Global intercomparison of functional pyrodiversity from two satellite sensors. Int. J. Rem. Sens. https://doi.org/10.1080/01431161.2021.1999529.

Moritz, M.A., Batllori, E., Bradstock, R.A., Gill, A.M., Handmer, J., Hessburg, P.F., Leonard, J., McCaffrey, S., Odion, D.C., Schoennagel, T., Syphard, A.D., 2014. Learning to coexist with wildfire. Nature 515 (7525), 58–66. https://doi.org/10.1038/nature13946.

Mouillot, F., Schultz, M.G., Yue, C., Cadule, P., Tansey, K., Ciais, P., Chuvieco, E., 2014. Ten years of global burned area products from spaceborne remote sensing—a review: analysis of user needs and recommendations for future developments. Int. J. Appl. Earth Obs. Geoinf. 26, 64–79. https://doi.org/10.1016/j.jag.2013.05.014.

Ngadze, F., Mpakairi, K.S., Kavhu, B., Ndaimani, H., Maremba, M.S., 2020. Exploring the utility of Sentinel-2 MSI and Landsat 8 OLI in burned area mapping for a heterogenous savannah landscape. PLoS One 15 (5), e0232962. https://doi.org/10.1371/journal.pone.0232962.

Nogueira, J.M.P., Ruffault, J., Chuvieco, E., Mouillot, F., 2017. Can we go beyond burned area in the assessment of global remote sensing products with fire patch metrics? Rem. Sens. 9 (1). https://doi.org/10.3390/rs9010007.

Olson, D.M., Dinerstein, E., Wikramanayake, E., Burgess, N., Powell, G.V.N., Underwood, E.C., Jennifer, A., Itoua, I., Strand, H.E., Morrison, J., Allnutt, T.F., Ricketts, T.H., Kura, Y., Lamoreux, J.F., Hedao, P., Kassem, K.R., 2001. Terrestrial ecoregions of the world: a new map of life on earth. Bioscience 51 (11), 933–938. https://doi.org/10.1641/0006-3568(2001)051[0933:teotwa]2.0.co;2.

Pacheco, A. da P., Silva, J. L. F. Da, Ruiz-Armenteros, A.M., Henriques, R.V.B., 2021. Assessment of K-nearest neighbor and random forest classifiers for mapping forest fire areas in Central Portugal using landsat-8, sentinel-2, and Terra imagery. Rem. Sens. https://doi.org/10.3390/rs13071345.

Padilla, M., Olofsson, P., Stehman, S.V., Tansey, K., Chuvieco, E., 2017. Stratification and sample allocation for reference burned area data. Rem. Sens. Environ. 203, 240–255. https://doi.org/10.1016/j.rse.2017.06.041.

Pathak, K., Nath, A.J., Sileshi, G.W., Lal, R., Das, A.K., 2017. Annual burning enhances biomass production and nutrient cycling in degraded imperata grasslands. Land Degrad. Dev. 28 (5), 1763–1771. https://doi.org/10.1002/ldr.2707.

Pelletier, C., Valero, S., Inglada, J., Champion, N., Dedieu, G., 2016. Assessing the robustness of random forests to map land cover with high resolution satellite image time series over large areas. Rem. Sens. Environ. https://doi.org/10.1016/j.rse.2016.10.010.

Pinto, M.M., Trigo, R.M., Trigo, I.F., DaCamara, C.C., 2021. A practical method for high-resolution burned area monitoring using sentinel-2 and VIIRS. Rem. Sens. 13 (9), 1608. https://doi.org/10.3390/rs13091608.

Potter, B.E., McEvoy, D.J., 2021. Weather factors associated with extremely large fires and fire growth days. Earth Interact. https://doi.org/10.1175/ei-d-21-0008.1.

Ramo, R., Roteta, E., Bistinas, I., van Wees, D., Bastarrika, A., Chuvieco, E., van der Werf, G.R., 2021. African burned area and fire carbon emissions are strongly

impacted by small fires undetected by coarse resolution satellite data. Proc. Natl. Acad. Sci. USA 118 (9). https://doi.org/10.1073/pnas.2011160118.
Randerson, J.T., Chen, Y., van der Werf, G.R., Rogers, B.M., Morton, D.C., 2012. Global burned area and biomass burning emissions from small fires. J. Geophys. Res.: Biogeosciences 117 (G4). https://doi.org/10.1029/2012JG002128 n/a-n/a.
Rostami, N., Heydari, M., Uddin, S.M.M., Borja, M.E.L., Lucas-Borja, M.E., 2022. Hydrological response of burned soils in croplands, and pine and oak forests in zagros forest ecosystem (western Iran) under rainfall simulations at micro-plot scale. In: Forests. https://doi.org/10.3390/f13020246.
Roteta, E., Bastarrika, A., Franquesa, M., Chuvieco, E., 2021. Landsat and sentinel-2 based burned area mapping tools in google earth engine. Rem. Sens. 13 (4), 816. https://doi.org/10.3390/rs13040816.
Roteta, E., Bastarrika, A., Ibisate, A., Chuvieco, E., 2021. A preliminary global automatic burned-area algorithm at medium resolution in google earth engine. Rem. Sens. 13 (21). https://doi.org/10.3390/rs13214298.
Roteta, E., Bastarrika, A., Padilla, M., Storm, T., Chuvieco, E., 2019. Development of a Sentinel-2 burned area algorithm: generation of a small fire database for sub-Saharan Africa. Rem. Sens. Environ. 222 (March), 1–17. https://doi.org/10.1016/j.rse.2018.12.011.
Roteta, E., Oliva, P., 2020. Optimization of a random forest classifier for burned area detection in Chile using sentinel-2 data. The International Archives of the Photogrammetry. Remote Sensing and Spatial Information Sciences 337–342. https://doi.org/10.5194/isprs-archives-xlii-3-w12-2020-337-2020. XLII-3/W12-2020.
Rouse, J.W., Haas, R.H., Schell, J.A., Deering, D.W., 1973. Monitoring vegetation systems in the great okains with ERTS. Third Earth Resources Technology Satellite-1 Symposium 1, 325–333.
Roy, D.P., Huang, H., Boschetti, L., Giglio, L., Yan, L., Zhang, H.H., Li, Z., 2019. Landsat-8 and Sentinel-2 burned area mapping - a combined sensor multi-temporal change detection approach. Rem. Sens. Environ. 231, 111254. https://doi.org/10.1016/j.rse.2019.111254.
Schneider, S.R., Lee, K., Santos, G., Abbatt, J.P.D., 2021. Air quality data approach for defining wildfire influence: impacts on PM 2.5 , NO 2 , CO, and O 3 in western Canadian cities. Environ. Sci. Technol. 55 (20), 13709–13717. https://doi.org/10.1021/acs.est.1c04042.
Schroeder, W., Giglio, L., 2018. NASA VIIRS Land Science Investigator Processing System (SIPS) Visible Infrared Imaging Radiometer Suite (VIIRS) 375 M & 750 M Active Fire Products: Product User's Guide (Issue July), Version 1.4.
Schroeder, W., Oliva, P., Giglio, L., Csiszar, I.A., 2014. The New VIIRS 375m active fire detection data product: algorithm description and initial assessment. Rem. Sens. Environ. 143, 85–96. https://doi.org/10.1016/j.rse.2013.12.008.
Seydi, S.T., Akhoondzadeh, M., Amani, M., Mahdavi, S., 2021. Wildfire damage assessment over Australia using sentinel-2 imagery and MODIS land cover product within the google earth engine cloud platform. Rem. Sens. 13 (2), 220. https://doi.org/10.3390/rs13020220.
Seydi, S.T., Hasanlou, M., Chanussot, J., 2022. Burnt-net: wildfire burned area mapping with single post-fire sentinel-2 data and deep learning morphological neural network. Ecol. Indicat. 140, 108999. https://doi.org/10.1016/j.ecolind.2022.108999.
Simon, M., 2004. Burnt area detection at global scale using ATSR-2: the GLOBSCAR products and their qualification. J. Geophys. Res. 109 (D14), D14S02. https://doi.org/10.1029/2003JD003622.
Simpson, J.E., Wooster, M.J., Smith, T.E.L., Trivedi, M., Vernimmen, R., Dedi, R., Shakti, M., Dinata, Y., 2016. Tropical peatland burn depth and combustion heterogeneity assessed using UAV photogrammetry and airborne LiDAR. Rem. Sens. https://doi.org/10.3390/rs8121000.
Smith, J.M., 2022. VIIRS Instruments Become More Essential As Terra and Aqua Drift from their Traditional Orbits, on NASA Earthdata. Updated May 18 2022, Retrieved May 19, 2024. https://www.earthdata.nasa.gov/learn/articles/modis-to-viirs-transition.
Stroppiana, D., Sali, M., Busetto, L., Boschetti, M., Ranghetti, L., Franquesa, M., Pettinari, M., Chuvieco, E., 2022. Sentinel-2 sampling design and reference fire perimeters to assess accuracy of Burned Area products over Sub-Saharan Africa for the year 2019. ISPRS J. Photogrammetry Remote Sens. 191, 223–234. https://doi.org/10.1016/j.isprsjprs.2022.07.015.
Szpakowski, D.M., Jensen, J.L.R., 2019. A review of the applications of remote sensing in fire ecology. Rem. Sens. https://doi.org/10.3390/rs11222638.
Tanase, M.A., Belenguer-Plomer, M.A., Roteta, E., Bastarrika, A., Wheeler, J., Fernández-Carrillo, Á., Tansey, K., Wiedemann, W., Navratil, P., Lohberger, S., Siegert, F., Chuvieco, E., 2020. Burned area detection and mapping: intercomparison of sentinel-1 and sentinel-2 based algorithms over tropical africa. Rem. Sens. 12 (2), 334. https://doi.org/10.3390/rs12020334.
Tansey, K., 2004. Vegetation burning in the year 2000: global burned area estimates from SPOT VEGETATION data. J. Geophys. Res. 109 (D14), D14S03. https://doi.org/10.1029/2003JD003598.
Teunissen, N., McAlpine, H., Cameron, S., Murphy, B.P., Peters, A., 2022. Demographic impacts of low- and high-intensity fire in a riparian savanna bird: implications for ecological fire management. https://doi.org/10.1101/2022.12.10.519856.
Trigg, S., Flasse, S., 2001. An evaluation of different Bi-spectral spaces for discriminating burned shrub-savannah. Int. J. Rem. Sens. https://doi.org/10.1080/01431160110053185.
Uda, S.K., Hein, L., Atmoko, D., 2019. Assessing the health impacts of peatland fires: a case study for Central Kalimantan, Indonesia. Environ. Sci. Pollut. Control Ser. 26 (30), 31315–31327. https://doi.org/10.1007/s11356-019-06264-x.
Urbanski, S., Nordgren, B., Albury, C., Schwert, B., Peterson, D., Quayle, B., Hao, W.M., 2018. A VIIRS direct broadcast algorithm for rapid response mapping of wildfire burned area in the western United States. Rem. Sens. Environ. 219, 271–283. https://doi.org/10.1016/j.rse.2018.10.007.
Valentini, R., Arneth, A., Bombelli, A., Castaldi, S., Cazzolla Gatti, R., Chevallier, F., Ciais, P., Grieco, E., Hartmann, J., Henry, M., Houghton, R.A., Jung, M., Kutsch, W. L., Malhi, Y., Mayorga, E., Merbold, L., Murray-Tortarolo, G., Papale, D., Peylin, P., et al., 2014. A full greenhouse gases budget of africa: synthesis, uncertainties, and vulnerabilities. Biogeosciences 11 (2), 381–407. https://doi.org/10.5194/bg-11-381-2014.
Van Der Werf, G.R., Randerson, J.T., Giglio, L., Collatz, G.J., Mu, M., Kasibhatla, P.S., Morton, D.C., Defries, R.S., Jin, Y., Van Leeuwen, T.T., 2010. Global fire emissions and the contribution of deforestation, savanna, forest, agricultural, and peat fires (1997-2009). Atmos. Chem. Phys. 10 (23), 11707–11735. https://doi.org/10.5194/acp-10-11707-2010.
Van Der Werf, G.R., Randerson, J.T., Giglio, L., Van Leeuwen, T.T., Chen, Y., Rogers, B. M., Mu, M., Van Marle, M.J.E., Morton, D.C., Collatz, G.J., Yokelson, R.J., Kasibhatla, P.S., 2017. Global fire emissions estimates during 1997-2016. Earth Syst. Sci. Data 9 (2), 697–720. https://doi.org/10.5194/essd-9-697-2017.
Van Wees, D., Van Der Werf, G.R., Randerson, J.T., Rogers, B.M., Chen, Y., Veraverbeke, S., Giglio, L., Morton, D.C., 2022. Global biomass burning fuel consumption and emissions at 500 m spatial resolution based on the Global Fire Emissions Database (GFED). Geosci. Model Dev. (GMD) 15 (22), 8411–8437. https://doi.org/10.5194/gmd-15-8411-2022.
Vermote, E., Justice, C., Csiszar, I., 2014. Early evaluation of the VIIRS calibration, cloud mask and surface reflectance Earth data records. Rem. Sens. Environ. 148, 134–145. https://doi.org/10.1016/j.rse.2014.03.028.
Vernooij, R., Giongo, M., Borges, M.A., Costa, M.M., Barradas, A.C.S., van der Werf, G.R., 2021. Intraseasonal variability of greenhouse gas emission factors from biomass burning in the Brazilian Cerrado. Biogeosciences 18 (4), 1375–1393. https://doi.org/10.5194/bg-18-1375-2021.
Voulgarakis, A., Field, R.W., 2015. Fire influences on atmospheric composition, air quality and climate. Current Pollution Reports. https://doi.org/10.1007/s40726-015-0007-z.
Wang, L., Diao, C., Xian, G., Yin, D., Lu, Y., Zou, S., Erickson, T.A., 2020. A summary of the special issue on remote sensing of land change science with Google earth engine. Rem. Sens. Environ. 248, 112002. https://doi.org/10.1016/j.rse.2020.112002.
Wang, P., Zhang, L., Zhang, G., Jin, B., Leung, H., 2019. Multispectral image super-resolution burned-area mapping based on space-temperature information. Rem. Sens. 11 (22), 2695. https://doi.org/10.3390/rs11222695.
Xie, Y., Lin, M., Decharme, B., Delire, C., Horowitz, L.W., Lawrence, D.M., Li, F., Séférian, R., 2022. Tripling of western US particulate pollution from wildfires in a warming climate. Proc. Natl. Acad. Sci. USA 119 (14). https://doi.org/10.1073/pnas.2111372119.
Xu, H., 2006. Modification of normalised difference water index (NDWI) to enhance open water features in remotely sensed imagery. Int. J. Rem. Sens. 27 (14), 3025–3033. https://doi.org/10.1080/01431160600589179.
Xu, H., Zhang, G., Zhou, Z., Zhou, X., Zhou, C., 2022a. Forest fire monitoring and positioning improvement at subpixel level: application to himawari-8 fire products. Rem. Sens. https://doi.org/10.3390/rs14102460.
Xu, H., Gui, Z., Zhou, Z., Zhou, X., Zhang, J., Zhou, C., 2022b. Development of a novel burned-area subpixel mapping (BASM) workflow for fire scar detection at subpixel level. Rem. Sens. 14 (15), 3546. https://doi.org/10.3390/rs14153546.
Zhao, H., Zhang, X., Zhang, S., Chen, W., Tong, D., Xiu, A., 2017. Effects of agricultural biomass burning on regional haze in China: a review. Atmosphere. https://doi.org/10.3390/atmos8050088.

References Appendix

Adole, T., Dash, J., Atkinson, P., 2018. Characterising the land surface phenology of Africa using 500 m Modis EVI. Appl. Geogr. 90, 187–199. https://doi.org/10.1016/j.apgeog.2017.12.006.
Laris, P., 2005. Spatiotemporal problems with detecting and mapping mosaic fire regimes with coarse-resolution satellite data in savanna environments. Rem. Sens. Environ. 99 (4), 412–424. https://doi.org/10.1016/j.rse.2005.09.012.
Laris, P., Wardell, D., 2006. Good, bad or 'necessary evil'? reinterpreting the colonial burning experiments in the savanna landscapes of west africa. Geogr. J. 172 (4), 271–290. https://doi.org/10.1111/j.1475-4959.2006.00215.x.
Linderman, M., Rowhani, P., Benz, D., Serneels, S., Lambin, É.F., 2005. Land-cover change and vegetation dynamics across africa. J. Geophys. Res. Atmos. 110 (D12). https://doi.org/10.1029/2004jd005521.
Smith, J., Stehman, S., Wickham, J., Yang, L., 2003. Effects of landscape characteristics on land-cover class accuracy. Rem. Sens. Environ. 84 (3), 342–349. https://doi.org/10.1016/s0034-4257(02)00126-8.
Stroppiana, D., Sali, M., Busetto, L., Boschetti, M., Ranghetti, L., 2022. Sentinel-2 sampling design and reference fire perimeters to assess accuracy of Burned Area products over Sub-Saharan Africa for the year 2019 ISPRS Journal of Photogrammetry and Remote Sensing Sentinel-2 sampling design and reference fire perimeters to as. ISPRS J. Photogrammetry Remote Sens. 191 (September), 223–234. https://doi.org/10.1016/j.isprsjprs.2022.07.015.